IEEE Access
Multidisciplinary ⋮ Rapid Review ⋮ Open Access Journal

Received January 20, 2022, accepted February 17, 2022, date of publication February 24, 2022, date of current version March 9, 2022.

Digital Object Identifier 10.1109/ACCESS.2022.3154386

Encoding and Tuning of THz Metasurface-Based Refractive Index Sensor With Behavior Prediction Using XGBoost Regressor

SHOBHIT K. PATEL[1], (Senior Member, IEEE), JAYMIT SURVE[2], (Graduate Student Member, IEEE), VIJAY KATKAR[1], JUVERIYA PARMAR[3,4], (Graduate Student Member, IEEE), FAHAD AHMED AL-ZAHRANI[5], KAWSAR AHMED[6,7], (Graduate Student Member, IEEE), AND FRANCIS MINHTHANG BUI[6], (Member, IEEE)

[1]Department of Computer Engineering, Marwadi University, Rajkot, Gujarat 360003, India
[2]Department of Electrical Engineering, Marwadi University, Rajkot, Gujarat 360003, India
[3]Department of Electronics and Communication Engineering, Marwadi University, Rajkot, Gujarat 360003, India
[4]Department of Mechanical and Materials Engineering, University of Nebraska–Lincoln, Lincoln, NE 68588, USA
[5]Computer Engineering Department, Umm Al-Qura University, Mecca 24381, Saudi Arabia
[6]Department of Electrical and Computer Engineering, University of Saskatchewan, Saskatoon, SK S7N 5A9, Canada
[7]Group of Biophotomatiχ, Department of Information and Communication Technology, Mawlana Bhashani Science and Technology University, Tangail 1902, Bangladesh

Corresponding authors: Kawsar Ahmed (kawsar.ict@mbstu.ac.bd) and Shobhit K. Patel (shobhitkumar.patel@marwadieducation.edu.in)

This work was supported in part by the Deanship of Scientific Research at Umm Al-Qura University under Grant 22UQU4170008DSR01, and in part by the Natural Sciences and Engineering Research Council of Canada (NSERC).

ABSTRACT We have investigated graphene-based three various refractive index sensors (split ring resonator (SRR), split ring resonator with thin wire (SRRTW), and thin wire (TW) refractive index sensors) for the encoding and sensing-based applications. The sensors are designed to detect the presence of hemoglobin biomolecules with high sensitivity. The results are analyzed in the form of transmittance, and electric field and detailed sensitivity analysis is also carried out for the proposed graphene-based refractive index sensors for four various concentrations of hemoglobin biomolecules. We have also investigated the sensor's performance in terms of quality factor, Q, and figure of merit (FOM). The encoding of '0' and '1' is attained by varying the graphene chemical potential fulfilling the one-digit coding. An array of these sensors can then be used for encoding-based applications. The detailed analysis of reported sensors is also carried out by checking the effect of varying physical parameters such as substrate thickness, split ring gap, and thin wire width on tunability. These sensors can be applied in biomedical or encoding-based applications. Experiments are performed using XGBoost regressor to determine, whether simulation time and resources can be reduced by using regression analysis to predict the transmittance values of intermediate frequency or not. Experimental results prove that regression analysis using XGBoost Regressor can reduce the simulation time and resources by at least 70 percent.

INDEX TERMS Encoding, graphene, refractive index sensor, machine learning, sensing, tunable, XGBoost regressor.

I. INTRODUCTION

Metamaterials have been the area of interest for decades due to their remarkable physical characteristics [1]. While studying the characteristics of metamaterials, Veselago [2] anticipated the extraordinary phenomenon associated with optical manipulation, biomimetic plastic, and effective thermoelectric materials [3]–[5]. The progressive research on metamaterial has been paced since the 21st century but is still in the primary stage. These metamaterials properties are due to the interaction between the structure and the incident electromagnetic waves. Even if there are various available technologies for biomarker sensing detection [6], [7] i.e., surface plasmon resonance (SPR) [8], localized surfacer plasmon resonance (LSPR) [9], surface-enhanced Raman scattering (SERS) [10] and terahertz (THz) [11]. THz wave's frequency range (0.1 THz to 10 THz) corresponds to the vibrational frequencies of various essential biomolecules [12]

The associate editor coordinating the review of this manuscript and approving it for publication was Aysegul Ucar.

such as proteins, RNA, DNA, making it possible to detect biomolecules vibrations. Terahertz spectroscopy has emerged as a potential technique for label-free, non-contact, and non-destructive analysis of chemical and biological compounds in recent years [13], [14]. The newly established portable THz spectroscopic tool, in particular, can detect and identify object materials on-site with a high signal-to-noise ratio [15], further promoting terahertz detection technology advancement. Although due to the low power of the terahertz source, the detection sensitivity available for quantitative and qualitative analysis is currently limited. Using a blend of metamaterial and terahertz time-domain spectroscopy devices to boost detection sensitivity is a smart option. This combination approach has been used by many researchers in the disciplines of medicine [16], [17], food safety [18], [19], and other fields.

Biosensors are used for multiple purposes including sensing, and encryption-based applications [20]–[22]. Biosensors are basically classified into labeled biosensors and label-free biosensors [23]. Due to the selectivity and affinity-like features, label-free biosensors are widely in demand. Hemoglobin biomolecules from blood can also be detected using label-free biosensors [24]. The sensing properties of label-free biosensors [25] are improved due to the recent advancements in carbon nanotubes and graphene material and as a reason, graphene is highly used for sensing applications [26]. In the diagnosis of bacterial and viral infections, biosensors are extremely quick and accurate [27], [28]. These diseases can also be detected with high sensitivity using grating sensors [29]. Photovoltaic devices, defense, and therapeutic applications can all benefit from graphene biosensors [30]. The graphene-based biosensor can also be constructed with a metasurface, which lowers the fabrication cost while providing good stability and sensitivity [31], [32]. Infrared and terahertz areas are well controlled by a graphene-based metamaterial sensor. They are cost-effective because they can be easily nanofabricated using the electron beam lithography technique [33]. In these metasurface-based graphene structures, optical properties including transmittance, absorption, and reflection aid in boosting overall sensitivity and efficiency [34]. Graphene sensors can be utilized for both encoding and decoding, allowing them to be employed in encryption applications.

Patel *et al.* presented a highly sensitive and tunable biosensor using phase change material for the detection of hemoglobin biomolecules with the sensitivity of 1000 nm/RIU [35]. The environmental crisis can also be analyzed using a graphene peptide-based absorber sensor [36]. Hemoglobin biomolecules with high sensitivity can also be detected using graphene-based leaky-wave optical absorber sensor design [37]. Raman signals at various combination which is used for biomedical diagnosis can also be detected using graphene gold nanoribbons substrate in an absorber sensor [38]. The basic parameters defining a sensor's performance are sensitivity, quality factor, Q, and figure of merit (FOM). Wang designed a sensor that achieved a Q factor of 14.2 and FOM of 3.3 [39]. Various biosensor applications have been discussed in detail by Patel and co-authors [40]. Barzegar-parizi *et al.* presented a refractive index sensor in which the absorptance bands were sensitive to the coating layer's refractive index [41]. Harnsoongneon *et al.* reported a glucose-composition detector based on a hybrid system of ELC resonator and coplanar waveguide, particularly for D-glucose sensing [42]. Varshney and co-authors presented a highly sensitive differential sensor based on ELC that can detect the purity of a product which is proved by detecting termite infestation in wood with 150 MHz of absolute sensitivity [43]. Li *et al.* presented a biosensor for the detection of ethanol solution using THz-based metamaterials and achieved the highest sensitivity of 112 GHz/RIU [44].

In this paper, we have explored three various graphene-based refractive index sensors of three different metasurface patterns of the split ring resonator, split ring resonator with thin wire, and thin wire. Among these three designs of refractive index sensors, we have achieved encoding and tuning characteristics for two designs that are split ring resonator and split ring resonator with thin wire refractive index sensors. For these designs, encoding is achieved by varying graphene chemical potential values for coding of '0' and '1'. We have also achieved the sensing properties that can help to detect hemoglobin biomolecules of four various concentrations. The designs and mathematical models of the sensors are presented in section II. Section III contains the detailed analysis of sensors w.r.t variation in different physical parameters and sensitivity, FOM, and Q factor analysis for all the proposed sensors. The encoding and tunability characteristics are illustrated in this section. Section IV contains a detailed description of behavior prediction using XGBoost Regressor. Behavior prediction can be used to reduce the simulation time and resources. Concluding notes are presented in section V.

II. DESIGN AND MODELING

The graphic illustrations of the split ring resonator graphene-based refractive index sensor are represented in Fig. 1. The proposed structure is varied for three resonator variations 1) Split ring resonator (SRR) design, 2) Split ring resonator with thin wire (SRRTW) design and 3) Thin wire (TW) design. The designs of SRR, SRRTW, and TW are represented in Fig. 1(a), Fig. 1(d), and Fig. 1(e), respectively. Fig. 1(b) and Fig. 1(c) represent the top view and front view of the proposed structure, respectively. The structures are designed by placing a ground plane of glass followed by various metasurface patterns using graphene material. The parameters of the designs are: the structure size, $L \times L$ is 10 μm $\times$ 10 μm, glass layer thickness, S_h, is 1.5 μm, thickness of hemoglobin layer, H_h, is 1.5 μm, the graphene material is allotted to the SRR, SRRTW, and TW and the height of graphene layer is set to 0.34 nm. The gap, h_g, of SRR is set to 0.5 μm, the width of SRR, W, is 3 μm, and the size of SRR, $C_L \times C_L$, is set as 8 μm $\times$ 8 μm, the length and width of thin wire, I_L and I_W, are 4 μm and 1 μm, respectively. Here we have designed a metasurface based refractive index sensor. For the structure to be metasurface, it is mandatory to have at

least one dimension less than or equal to lambda/4, lambda being the wavelength of operation. In the same manner, all the sensors can be designed. Split ring resonator (SRR) design is having a gap that provides capacitive effect which is required for metasurface enabled sensors. The comparison of the same design is also provided with the less capacitive thin wire (TW) design. The sensitivity should be higher for substrates with lower permittivity [45].

Sensitivity is calculated by measuring the difference between the peak of two biomolecules and used as a performance measure for sensors. As the difference between peak increases the quality of the sensor is increased due to the improved sensitivity. Sensitivity can be calculated using the following equation (1) [46]:

$$S = \frac{\Delta f}{\Delta n} \tag{1}$$

where Δf is the frequency difference between two transmittance peaks and Δn is the difference of refractive index between these two points.

A figure of merit (FOM) is the ratio of the sensitivity and the resonance frequency line width which is highly used to specify sensing proficiency. FOM is described as [47]:

$$FOM = \frac{S}{FWHM} \tag{2}$$

where s stands for the sensitivity and the FWHM indicates the full width at half maximum.

A quality factor Q is another merit to ensure sensor's performance and it is defined as [44]:

$$Q = \frac{f_r}{FWHM} \tag{3}$$

The conductivity σ_s of graphene is derived from equations (1-4) [48]

$$\varepsilon(\omega) = 1 + \frac{\sigma_s}{\varepsilon_0 \omega \nabla} \tag{4}$$

$$\sigma_{intra} = \frac{-je^2 k_B T}{\pi \hbar^2 (\omega - j2\Gamma)} \left(\frac{\mu_c}{k_B T} + 2\ln\left(e^{\frac{\mu_c}{k_B T}} + 1\right)\right) \tag{5}$$

$$\sigma_{inetr} = \frac{-je^2}{4\pi\hbar} \ln\left(\frac{2|\mu_c| - (\omega - j2\Gamma)\hbar}{2|\mu_c| + (\omega - j2\Gamma)\hbar}\right) \tag{6}$$

$$\sigma_s = \sigma_{intra} + \sigma_{inter} \tag{7}$$

where permittivity is indicated using ε, vacuum's permittivity is indicated by ε_0, angular frequency is labeled as ω, and the thickness of the monolayer graphene sheet is labeled as ∇. The conductivity of graphene can be classified into two different parts, intraband conductivity (σ_{intra}) and interband conductivity (σ_{inetr}). Boltzmann's constant is indicated by its usual symbol, k_B, $\hbar$ stands for the reduced plank's constant, room temperature is labeled as T, and the graphene chemical potential indicated by μ_c, can be defined as $\mu_c = \hbar v_F \sqrt{\pi C V_{DC}/e}$, where the gate voltage is labeled as V_{DC}, v_F is identified as the Fermi velocity, and C stands for the capacitance.

The permittivity and permeability equations of metasurfaces are presented in equations (6-10). These parameters

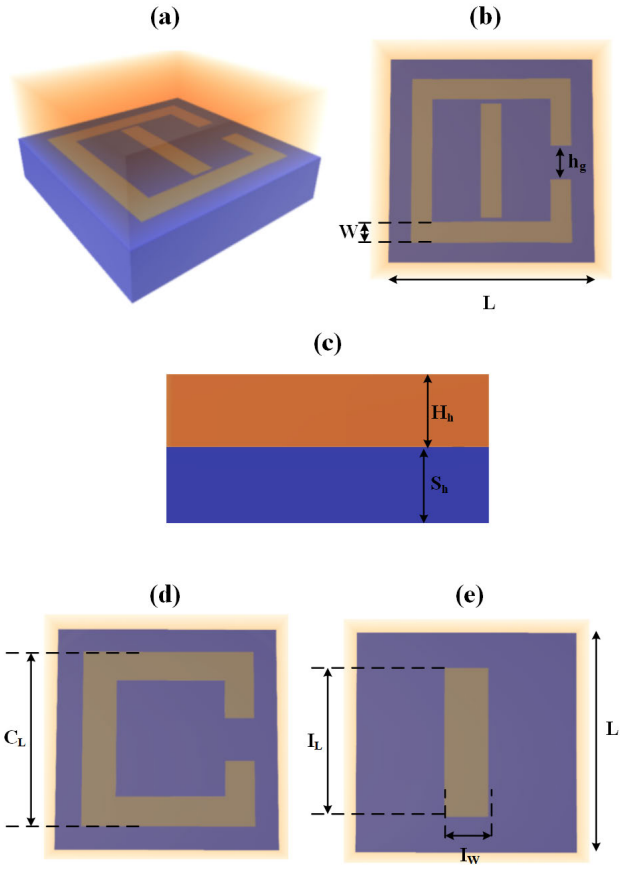

FIGURE 1. Illustrations of THz metamaterial-based refractive index sensor (a) 3D view of SRRTW sensor design, (b) top view of SRRTW sensor design, (c) front view of SRRTW sensor design, (d) top view of SRR sensor design, (e) top view of TW sensor design.

are obtained from the impedance and the refractive index as presented in the equations [49]:

$$z = \pm\sqrt{\frac{(1+S_{11})^2 - S_{21}^2}{(1-S_{11})^2 - S_{21}^2}} \tag{8}$$

$$e^{ink_0 d} = \frac{S_{21}}{1 - S_{11}\frac{z-1}{z+1}} \tag{9}$$

$$n = \frac{1}{k_0 d}\left[\left\{\left[\ln\left(e^{ink_0 d}\right)\right]'' + 2m\pi\right\} - i\left[\ln\left(e^{ink_0 d}\right)\right]'\right] \tag{10}$$

$$\varepsilon = \frac{n}{z} \tag{11}$$

$$\mu = nz \tag{12}$$

where the impedance is referred to as z, S_{11} and S_{21} are referred to reflection and transmission coefficients, respectively, the refractive index is labeled as n, the maximum length of the unit element is labeled as d, wavenumber is labeled using k_0, a branch due to the periodic characteristics of sinusoidal function is labeled using m, permittivity and permeability are labeled by their usual symbols, ε, and μ, respectively.

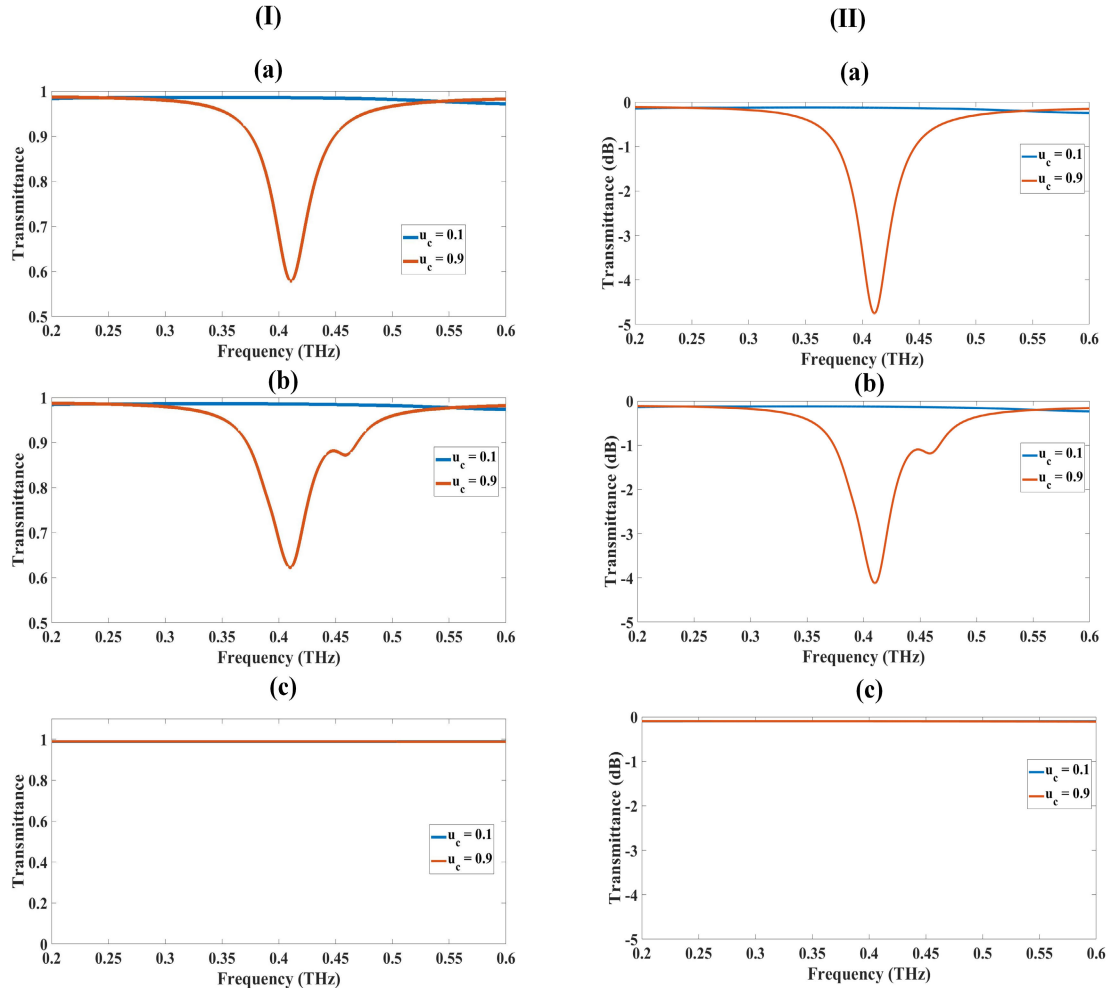

FIGURE 2. Transmittance band for proposed refractive index sensors for various GCP values where 0.1 eV and 0.9 eV can be encoded as '0' and '1', respectively. GCP variation for (I) in normalized scale: (a) SRR sensor design, (b) SRRTW sensor design, and (c) TW sensor design. (II) in dB scale: (a) SRR sensor design, (b) SRRTW sensor design, and (c) TW sensor design.

III. RESULTS AND DISCUSSION

Designs presented in Fig. 1 are simulated using COMSOL Multiphysics software using Finite Element Method (FEM) and the results in the terms of transmittance and electric field are reported in Fig. 2-8. The transmittance plots of all the three designs SRR, SRRTW, and TW refractive index sensors are illustrated in Fig.2 for the frequency range of 0.2 THz to 0.6 THz, respectively. The plot shows the transmittance plot for all three designs for two different values of graphene chemical potential (GCP) of 0.1 eV and 0.9 eV, respectively. For SRR refractive index sensor, the transmittance drops to 0.578 for GCP of 0.9 eV at the frequency value of 0.411 THz and for GCP value of 0.1 eV, the near-perfect transmittance is achieved as observed in Fig. 2 (a). The same phenomena follow for the SRRTW refractive index sensor. For SRRTW the transmittance value drops to 0.622 at 0.41 THz for the GCP of 0.9 eV and the near-unity transmittance is achieved for the GCP value of 0.1 eV as observed in Fig. 2(b). For the TW refractive index sensor, we only achieved the near-perfect transmittance response for both the values of GCP of 0.1 eV and 0.9 eV. As represented in Fig. 2(c), there is no drop in the transmittance plot for the TW sensor in the frequency range of 0.2 THz to 0.6 THz. Due to the drop at 0.9 eV GCP value, we can use SRR and SRRTW refractive index sensors as encoders as the GCP values of 0.1 eV and 0.9 eV can be encoded as '0' and '1', respectively. Fig. 2(I) and Fig. 2(II) are provided for two different scales including normalized and dB, respectively. This concept can be expanded by producing an array of these sensors and can be used to code the entire surface with various codes. This coded surface can be used to generate the signal that will be transmitted and decoded by another coded surface.

Later we checked if the tuning can be achieved using varying some of the physical parameters such as SRR and SRRTW gap, the width of TW, substrate thickness, etc., and the particular results are presented in Fig. 3 and Fig. 4, respectively. Fig.3 (a), (c) illustrates the variation in transmittance plot w.r.t to increment in the split ring gap of SRR, and

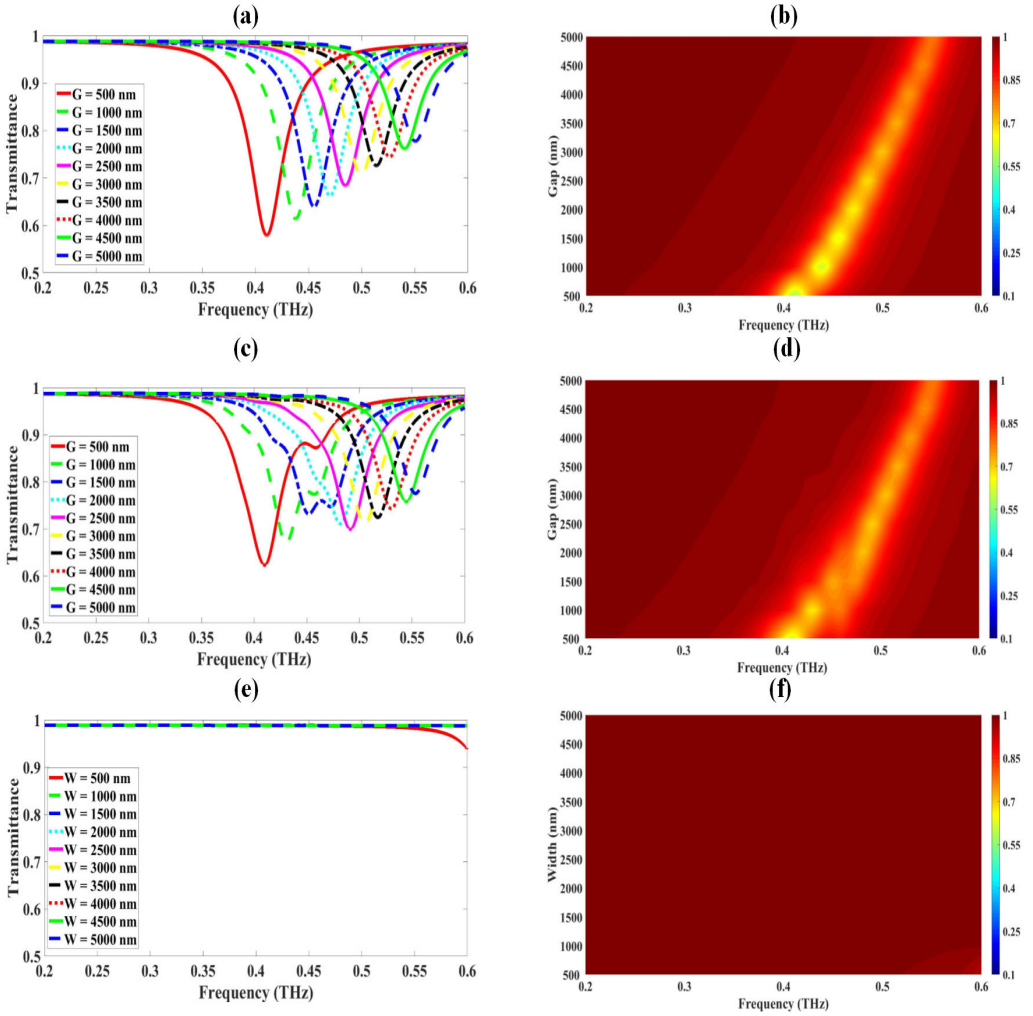

FIGURE 3. Variation in transmittance band for proposed refractive index sensor (a) variation in transmittance w.r.t variation in the gap of SRR. (b) The right shift and increment in transmittance are observed as the gap of SRR is increased as observed in the fermi energy plot. (c) variation in transmittance w.r.t variation in the gap of SRRTW. (d) The right shift and increment in transmittance are observed as the gap of SRRTW is increased as observed in the fermi energy plot. (e) variation in transmittance w.r.t variation in the width of TW. There is no variation in transmittance for the given frequency range for TW refractive index sensor. (f) There is no variation in transmittance except for W = 500 nm w.r.t increment in width of TW as observed in the fermi energy plot.

SRRTW refractive index sensor design, respectively. Fig. 3(e) represents the variation in transmittance plot w.r.t change in the width of the TW refractive index sensor. It is observed from Fig. 3(a) that for SRR refractive index sensor, as the gap of the split ring is increased, the transmittance starts to shift towards the right and the transmittance starts to increase as well. The highest drop of 0.578 in transmittance is achieved for the split ring gap of 500 nm and it gradually decreases as the split ring gap is varied in the range of 500 nm to 5000 nm in the step of 500 nm. The right shift and increment in transmittance are clearly visible in the fermi energy plot presented in Fig. 3(b). The main reason behind the transmission shift is as we increase the SRR gap, due to the capacitive effect the resonance changes which in a way affect the transmission response. Due to this reason as we increase the SRR gap the transmission shifts towards the right. It is deduced from Fig. 3(c) that for the SRRTW refractive index sensor, as the split ring gap is increased, the transmittance starts to shift towards the right and the transmittance starts to increase as well. The highest drop of 0.622 in transmittance is achieved for the split ring gap of 500 nm and it gradually decreases as the split ring gap is varied in the range of 500 nm to 5000 nm in the step of 500 nm. The right shift and increment in transmittance are clearly visible in the fermi energy plot presented in Fig. 3(d). It is observed in Fig. 3(e) that there is no effect of increasing TW width on transmittance plot in the frequency range of 0.2 THz to 0.6 THz. A slight drop is achieved at the end of the band for the thin wire width of 500 nm which is observable in Fig. 3(f).

Fig. 4 shows the variation in transmittance w.r.t substrate thickness for all the three SRR, SRRTW, and TW refractive index sensor designs. Substrate thickness is varied from

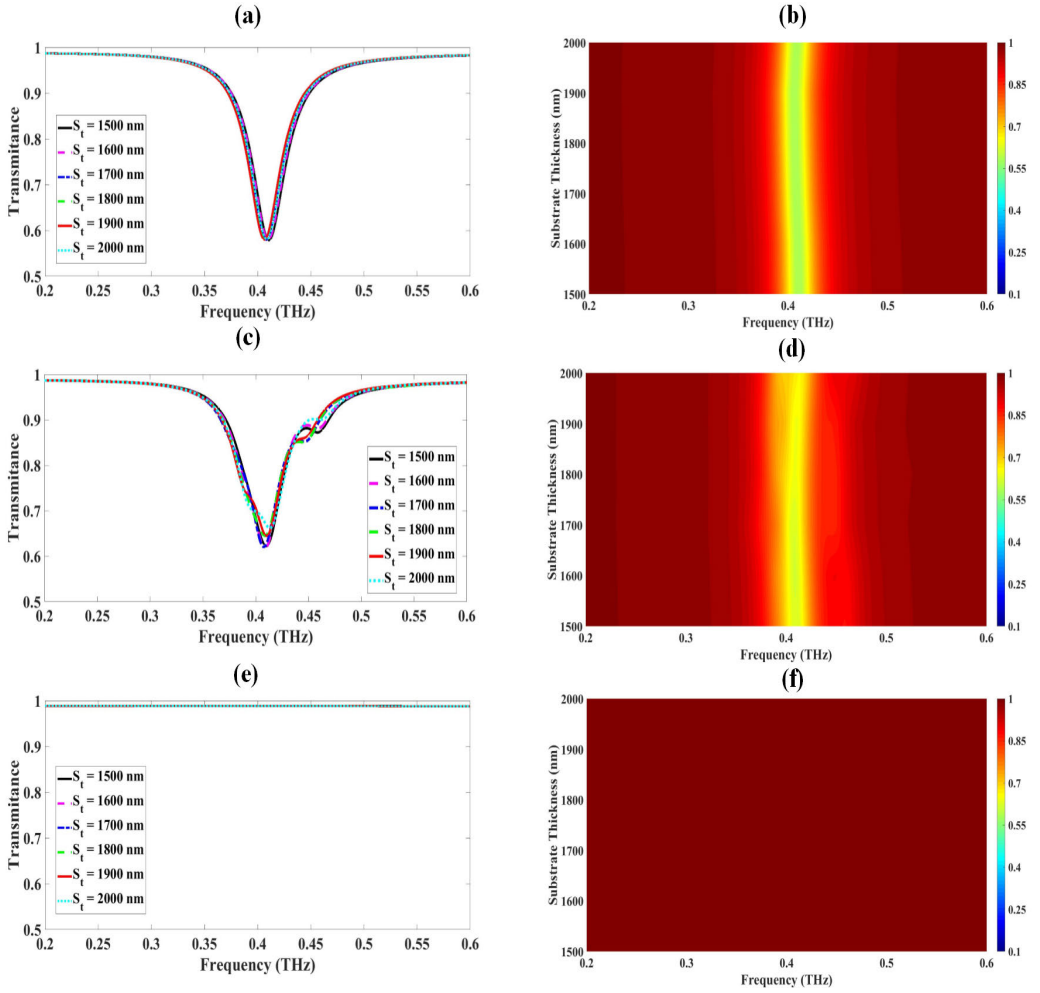

FIGURE 4. Variation in transmittance band for proposed refractive index sensor (a) variation in transmittance w.r.t variation in substrate thickness of SRR. (b) There is no variation in transmittance band but as substrate thickness reaches 1900 nm transmittance slightly shifts right as observed in the fermi energy plot. (c) variation in transmittance w.r.t variation in substrate thickness of SRRTW. (d) There is no variation in transmittance band but as substrate thickness reaches 1800 nm transmittance slightly shifts right as observed in the fermi energy plot. (e) variation in transmittance w.r.t variation in substrate thickness of TW. There is no variation in transmittance for the given frequency range for TW refractive index sensor. (f) There is no variation in transmittance w.r.t increment in substrate thickness of TW as observed in the fermi energy plot.

1500 nm to 2000 nm with the step increment of 100 nm and the results are obtained for the frequency range of 0.2 THz to 0.6 THz. Fig. 4(a) shows the change in transmittance plot w.r.t increment in substrate thickness for SRR refractive index sensor. It is observed that there is a very slight change in transmittance as we increase the substrate thickness.

The Fermi plot represented in Fig. 4(b) indicates the slight right shift in transmittance plot after substrate thickness reaches 1900 nm. The variation in transmittance plot w.r.t increasing substrate thickness for SRRTW refractive index sensor is reported in Fig. 4(c). It is observed that there is a very slight change in transmittance as we increase the substrate thickness. The plot also indicates that the transmittance drop starts to reduce slightly as the substrate thickness reaches 1800 nm which can also be observed in Fig. 4(d). Fermi plot represented in Fig. 4(d) also indicates the slight right shift in transmittance plot after substrate thickness reaches 1800 nm. The change in transmittance plot w.r.t increasing substrate thickness for TW refractive index sensor is reported in Fig. 4(e). It is observed that there is no change in transmittance as we increase the substrate thickness which can also be observed in the fermi plot represented in Fig. 4(f). Thus, We achieved the optimal structural parameters to achieve maximum sensitivity that is SRR gap G = 500 nm, and substrate thickness, $S_t = 1500$ nm. We have also checked the impact of the angle of incidence on the transmittance plot to verify if the transmittance reaches unity or not for any angle for all the three refractive index sensor designs and the related results are reported in Fig. 5. The results were obtained for the angle of incidence from 0° to 80° with the step increment of 10°. Fig. 5(a) shows the impact of the angle of incidence on the transmittance plot for the SRR

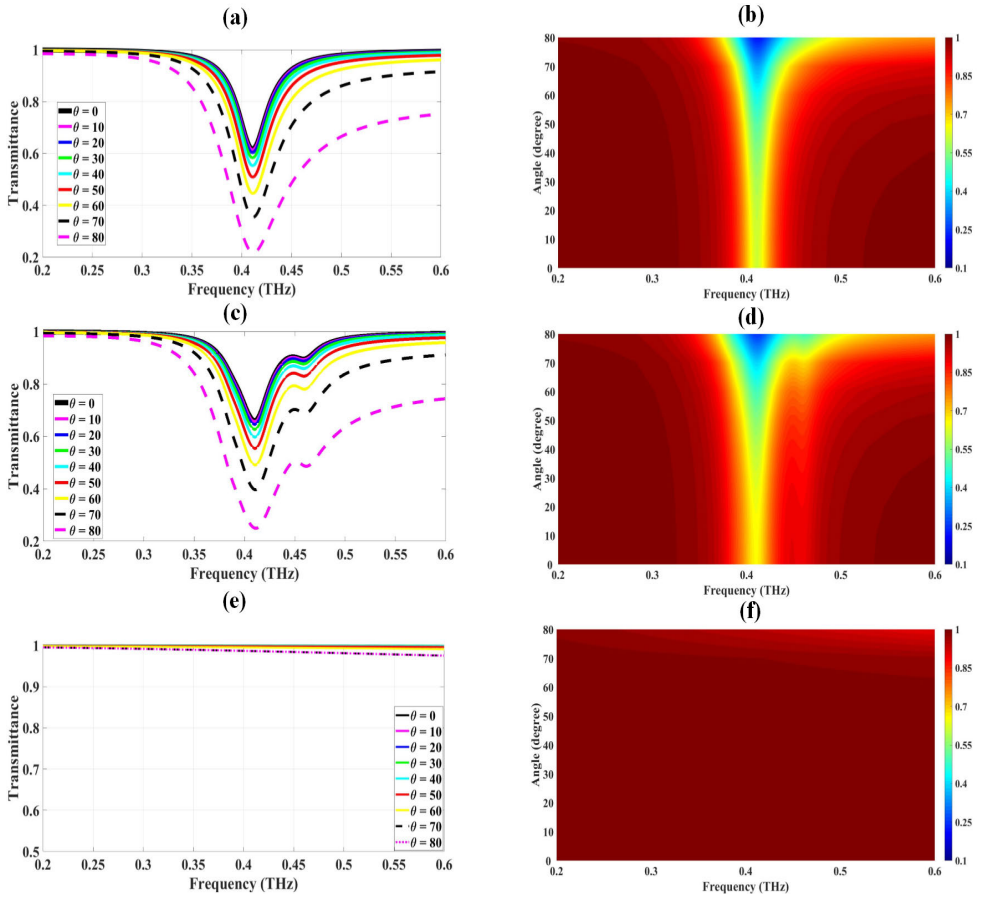

FIGURE 5. Variation in transmittance band for proposed refractive index sensor (a) variation in transmittance w.r.t variation in the angle of incidence for SRR. (b) The decrement in transmittance is observed as the angle of incidence for SRR is increased as observed in the fermi energy plot. (c) variation in transmittance w.r.t variation in the angle of incidence for SRRTW. (d) The decrement in transmittance is observed as the angle of incidence for SRRTW is increased as observed in the fermi energy plot. (e) variation in transmittance w.r.t variation in the angle of incidence for TW. There is no variation in transmittance for the given frequency range for TW refractive index sensor. (f) There is no variation in transmittance except for $\theta = 70°$, $80°$ w.r.t increment in the angle of incidence for TW as observed in the fermi energy plot.

TABLE 1. Analysis of sensitivity of proposed refractive index sensors for the various concentration of hemoglobin.

Parameters		Hemoglobin Biomolecules			
		n1	n2	n3	n4
		1.34	1.36	1.39	1.43
Δn		0.02	0.03		0.04
Split ring resonator design	f (THz)	0.411	0.408	0.405	0.400
	Δf (GHz)	3	3		5
	S = Δf/Δn (GHz/RIU)	**150**	100		125
Split ring resonator and thin wire design	f (THz)	0.410	0.408	0.404	0.399
	Δf (GHz)	2	4		5
	S = Δf/Δn (GHz/RIU)	100	**133**		125

TABLE 2. Sensor's performance analysis in terms of q factor and FOM.

Refractive Index Sensor Design	Sensitivity (S) (GHz/RIU)	Resonance Frequency (f_r) (in THz)	FWHM (THz)	Q factor	FOM
Split ring resonator design (SRR)	150	0.411	0.039	10.54	3.85
Split ring resonator with thin wire design (SRRTW)	133	0.410	0.044	9.32	3.02

refractive index sensor. It is observed that the transmittance drop starts to increase as the angle of incidence increases as we can observe in Fig. 5(b). The highest transmittance drop is observed for 80° and the transmittance drops to 0.217 at 0.411 THz. Fig. 5(c) shows the effect of angle of incidence

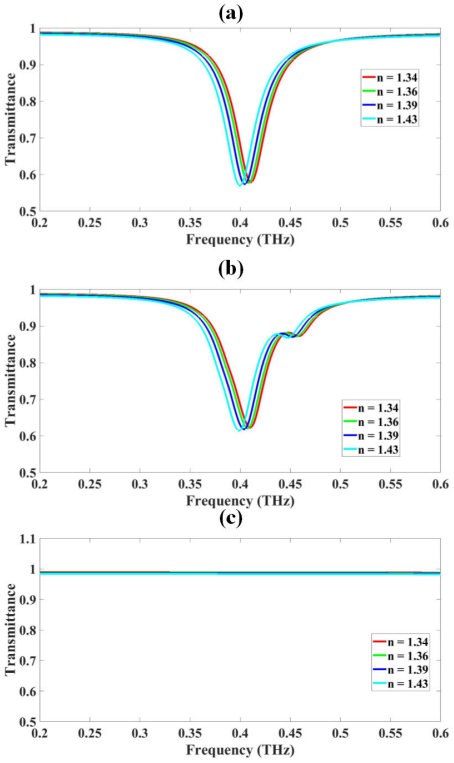

FIGURE 6. Transmittance band for proposed refractive index sensors for the various concentration of hemoglobin of 10 g/l, 20 g/l, 30 g/l, 40 g/l with refractive indices of 1.34 RIU, 1.36 RIU, 1.39 RIU, 1.43 RIU, respectively. variation of transmittance spectrum for the various concentration of hemoglobin in the frequency range of 0.2 THz to 0.6 THz for (a) SRR sensor design, (b) SRRTW sensor design, and (c) TW sensor design.

TABLE 3. Comparison table of proposed structures with previously published work.

Sensor Design	Frequency/ Wavelength range	Sensitivity	Application
Proposed Split ring resonator design (SRR)	0.2 THz – 0.6 THz	150 GHz/RIU	Hemoglobin detection, Encoding
Proposed Split ring resonator with thin wire design (SRRTW)	0.2 THz – 0.6 THz	133 GHz/RIU	Hemoglobin detection, Encoding
Ref [54]	1.15-1.3 µm	1421 nm/RIU	Hemoglobin Detection
Ref [55]	0.4 THz – 1 THz	33 GHz/RIU	
Ref [56]	-	387 nm/RIU	Hemoglobin Detection
Ref [57]	0.9 – 1.2 µm	294 nm/RIU	Biosensor, Slow-light devices
Ref [58]	115 – 215 THz	929 nm/RIU	Sensing in chemical, and biological diagnosis
Ref [59]	380 – 460 THz	700 nm/RIU	Sensing
Ref [60]	0.7 – 0.85 µm	3500 nm/RIU	Hemoglobin Detection
Ref [61]	1.55 – 1.58 µm	322 nm/RIU	Biosensing
Ref [62]	0.5 – 0.75 µm	1139 nm/RIU	Sensing
Ref [63]	1.37 – 1.45 µm	65.7 nm/RIU	Biochemical Sensing

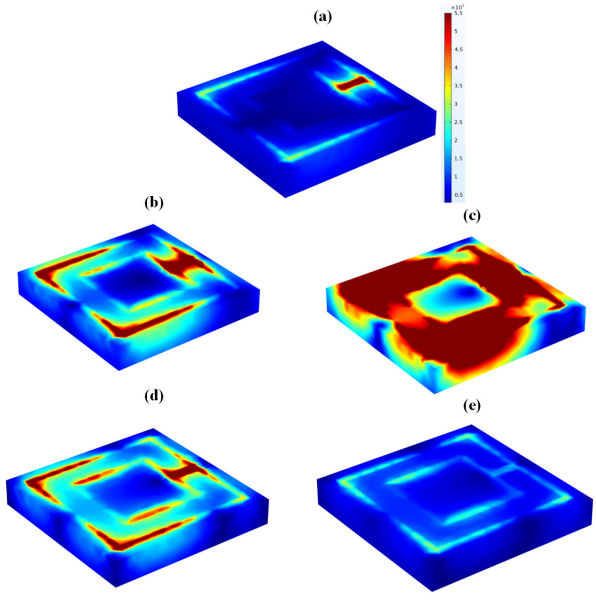

FIGURE 7. Electric field intensity for SRR refractive index sensor for various frequencies (a) 0.2 THz, (b) 0.35 THz, (c) 0.41 THz, (d) 0.48 THz, (e) 0.6 THz.

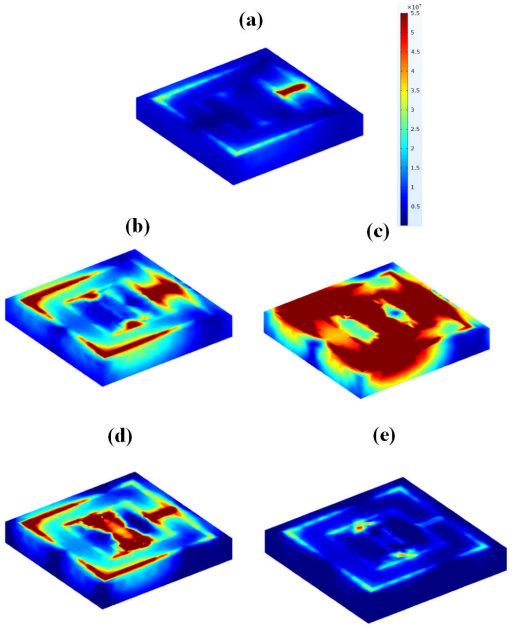

FIGURE 8. Electric field intensity for SRRTW refractive index sensor for various frequencies (a) 0.2 THz, (b) 0.35 THz, (c) 0.41 THz, (d) 0.48 THz, (e) 0.6 THz.

on transmittance plot for SRRTW refractive index sensor. The same phenomenon of the transmittance drop to increase as the angle of incidence increases follows here as we can observe in Fig. 5(d). The highest transmittance drop is observed for 80° and the transmittance drops to 0.249 at 0.411 THz. Fig. 5(e) shows the effect of angle of incidence on transmittance plot

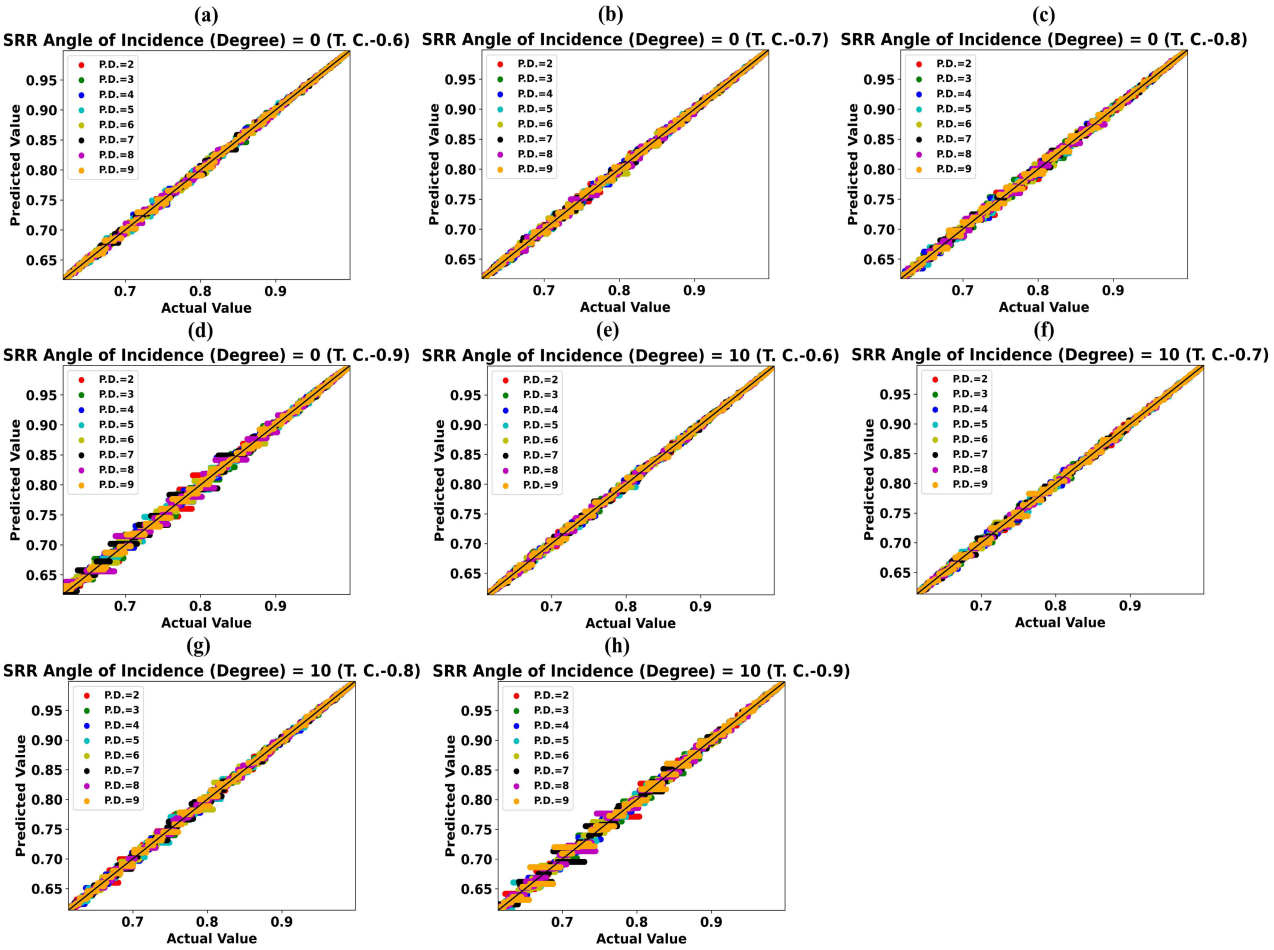

FIGURE 9. Predicted absorption value by XGBoost regressor vs. actual absorption value for SRR angle of incidence (a) 0° (T.C.-0.6) (b) 0° (T.C.-0.7) (c) 0° (T.C.-0.8) (d) 0° (T.C.-0.9) (e) 10° (T.C.-0.6) (f) 10° (T.C.-0.7) (g) 10° (T.C.-0.8) (h) 10° (T.C.-0.9).

for TW refractive index sensor. It is observed that the transmittance remains at near-unity as the angle of incidence increases and slightly decreases for the angle of incidence of 70°, and 80° as we can observe in Fig. 5(e) and 5(f). The proposed refractive index sensor is wide-angle insensitive for 0° to 60° which is a plus point of the proposed structure. Many previously available works are not so wide-angle insensitive [50]–[53]. Our structure's transmittance response varies (20% to 30%) only for the angle of incidence of 70° and 80°. To resolve this issue, we can construct a platform to avoid the incidence of the rays at these particular angles and achieve the proper transmittance response and avoid cross-sensitivity, and in the same manner the measurement error.

The standard range used for hemoglobin and urine biomolecule concentrations is 10 g/l, 20 g/l, 30 g/l, 40 g/l, 50 g/l, 60 g/l, and so on. For the purpose of this experiment, we have used the first four of these concentrations for hemoglobin biomolecules with refractive indices of 1.34 RIU, 1.36 RIU, 1.39 RIU, 1.43 RIU, respectively and the particular results for all three designs are presented in Fig. 6. The variation in the transmittance plot is clearly visible for the various concentration of hemoglobin and sensitivity analysis is also carried out for all the three SRR, SRRTW, and TW refractive index sensors. The detailed sensitivity analysis is also presented in the form of a table in Table 1 and the sensitivity is calculated from the change in transmittance drop at various frequencies and the change in the refractive index for those particular drops. The results for SRR refractive index sensor are reported in Fig. 6(a) and the maximum sensitivity of 150 GHz/RIU is achieved. The same analysis for the SRRTW refractive index sensor is carried out and the related result is illustrated in Fig. 6(b). The maximum sensitivity of 133 GHz/RIU is achieved for this particular design. It is distinctly clear from Fig. 6(c) that there is no tuning observed for the TW refractive index sensor in the frequency range of 0.2 THz to 0.6 THz. From Fig. 6 and Table 1, it is evidently clear that the highest tuning of 150 GHz/RIU is achieved for SRR refractive index sensor design.

The electric field results for SRR refractive index sensor are reported in Fig. 7. Five results for various frequencies

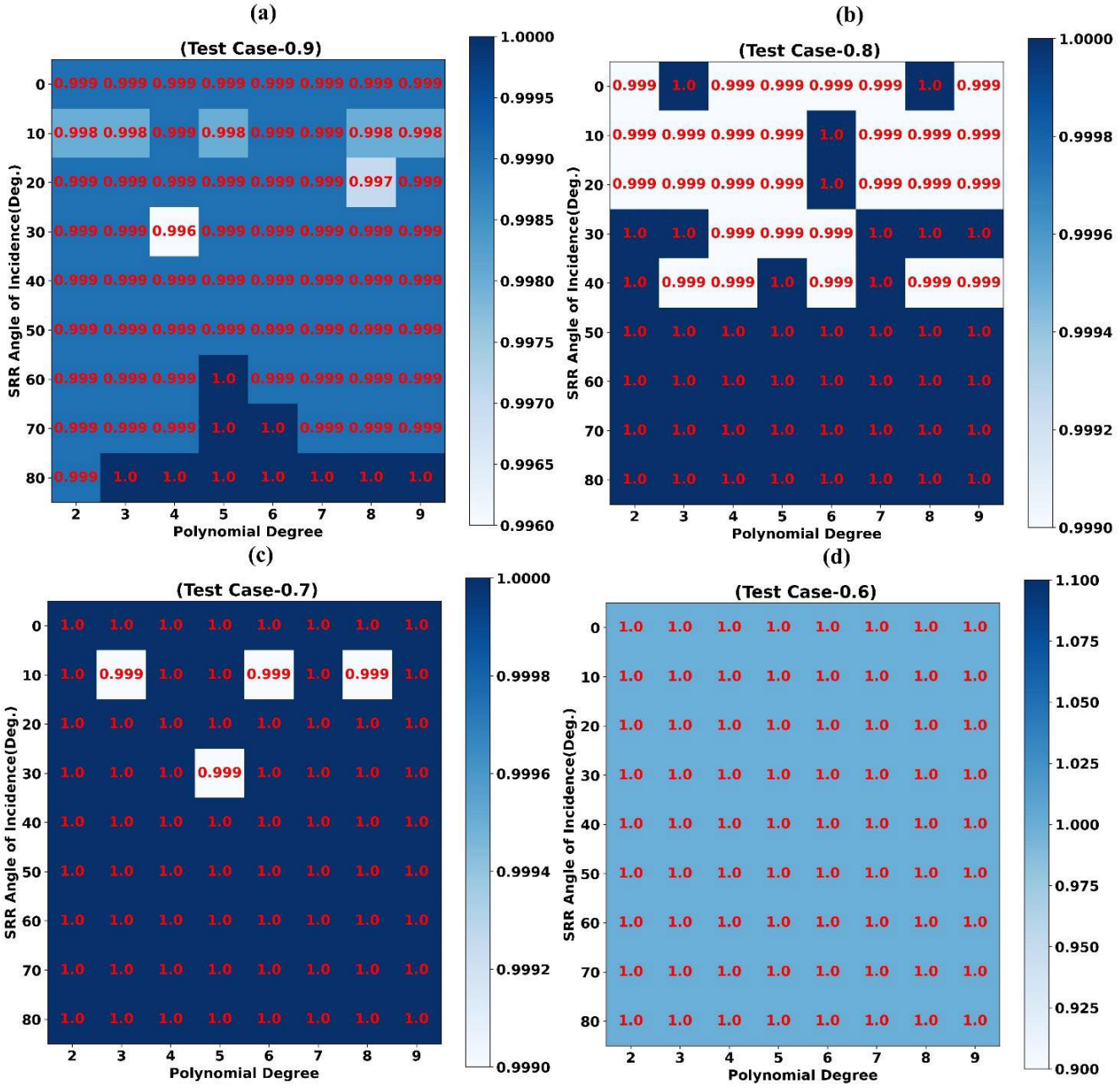

FIGURE 10. Prediction accuracy (R^2 Score) of XGBoost Regressor models trained for various values of SRR angle of incidence and (a) Test Case T.C.-0.9 (b) Test Case T.C.-0.8 (c) Test Case T.C.-0.7 (d) Test Case T.C.-0.6.

are illustrated and these frequencies are chosen to showcase the behavior of the sensor for the selected frequency range of 0.2 THz to 0.6 THz. We have selected five various frequencies from this span 0.2 THz, 0.35 THz, 0.411 THz, 0.48 THz, and 0.6 THz. It is distinctly clear that as the frequency reaches from 0.2 THz to 0.411 THz the absorption gradually increases due to the decrement in transmittance. And the absorption starts to reduce as frequency reaches from 0.411 THz to 0.6 THz due to the near-unity transmittance response. We can see the red color indicating the absorption of a wave near the metasurface in Fig. 7(c) for 0.411 THz frequency. The electric field results of the SRRTW refractive index sensor are presented in Fig. 8 for five various frequencies of 0.2 THz, 0.35 THz, 0.410 THz, 0.48 THz, 0.6 THz. It is distinctly clear that as the frequency reaches from 0.2 THz to 0.410 THz the absorption increases gradually because of the decrement in transmittance. Meanwhile, the absorption starts to reduce as frequency reaches from 0.410 THz to 0.6 THz due to the near-unity transmittance response. We can see the red color indicating the absorption of a wave near the metasurface in Fig. 7(c) and 8(c) for 0.411 THz frequency.

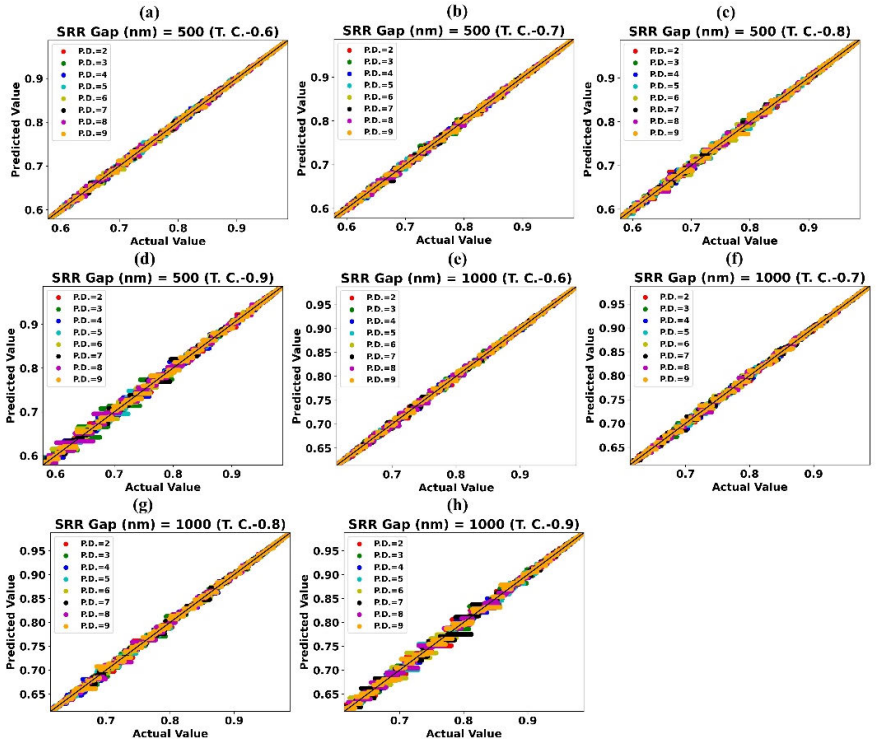

FIGURE 11. Predicted absorption value by XGBoost regressor vs. actual absorption value for SRR gap (nm) (a) 500 (T.C.-0.6) (b) 500 (T.C.-0.7) (c) 500 (T.C.-0.8) (d) 500 (T.C.-0.9) (e) 1000 (T.C.-0.6) (f) 1000 (T.C.-0.7) (g) 1000 (T.C.-0.8) (h) 1000 (T.C.-0.9).

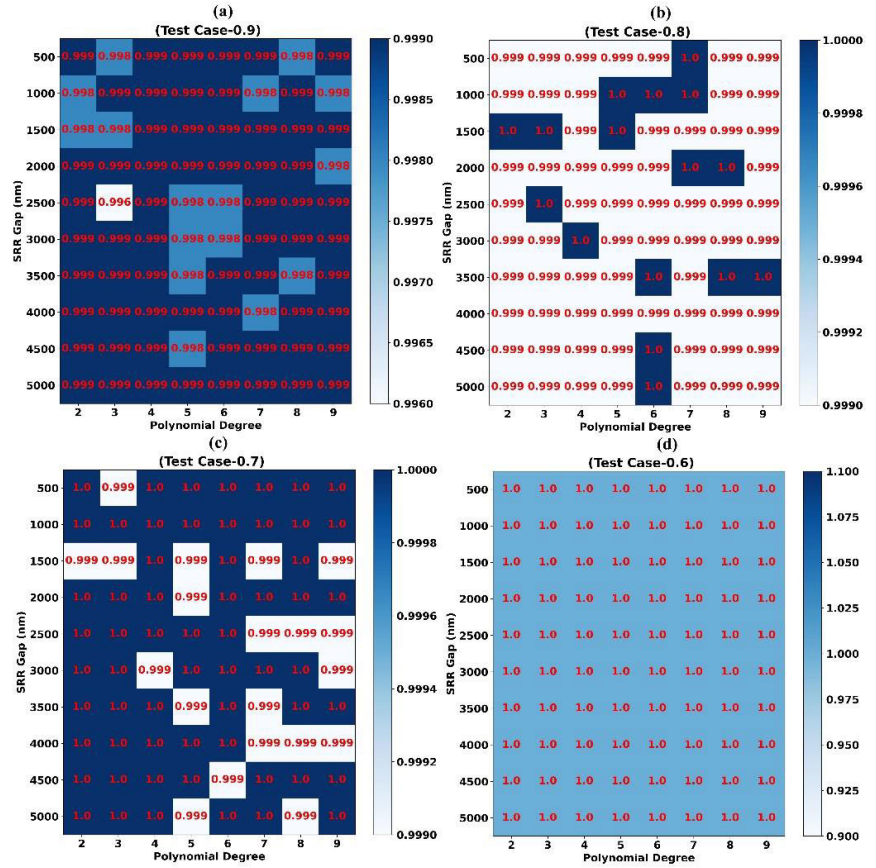

FIGURE 12. Prediction accuracy (R^2 Score) of XGBoost Regressor models trained for various values of SRR gap and (a) Test Case T.C.-0.9 (b) Test Case T.C.-0.8 (c) Test Case T.C.-0.7 (d) Test Case T.C.-0.6.

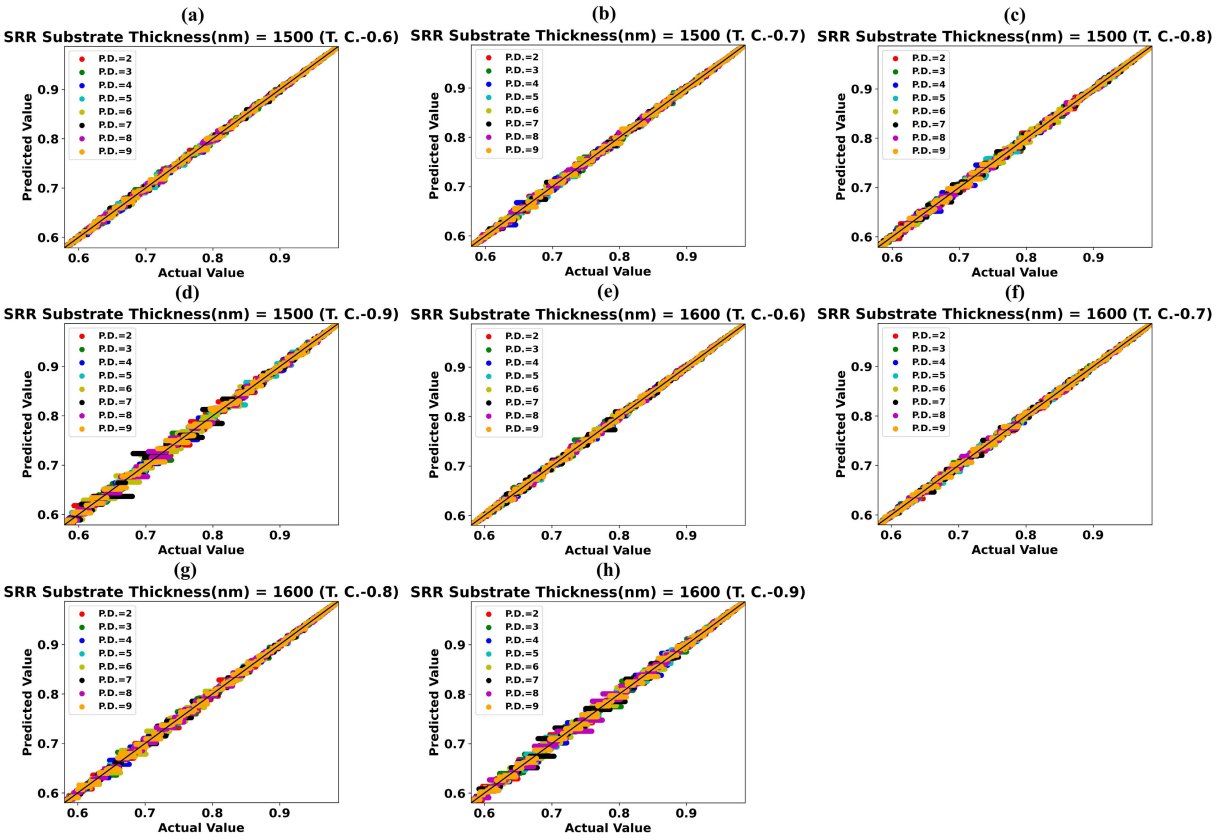

FIGURE 13. Predicted absorption value by XGBoost regressor vs. actual absorption value for SRR substrate thickness (nm) (a) 1500 (T.C.-0.6) (b) 1500 (T.C.-0.7) (c) 1500 (T.C.-0.8) (d) 1500 (T.C.-0.9) (e) 1600 (T.C.-0.6) (f) 1600 (T.C.-0.7) (g) 1600 (T.C.-0.8) (h) 1600 (T.C.-0.9).

We have also justified the sensor's performance using the main parameters such as the figure of merit and quality factor, Q. The detailed analysis is shown in Table 2. In recent times, researchers are investigating the highly sensitive metamaterial structures with high Q value and low FOM. From the results obtained in Table 2, we can indistinctly deduce that the proposed SRR and SRRTW refractive index sensors are highly sensitive with high Q factor and low FOM as we have achieved the Q factor of 10.54 and 9.32 and FOM of 3.85 and 3.02 for SRR and SRRTW refractive index sensors, respectively. We have combined the TW and SRR arrays for the purpose of comparing the results of all three structures. And it is clear from the results that for desired frequency range, the SRR resonators are achieving better sensitivity compared to the other two structures. Thus, it is clear that the proposed SRR and SRRTW refractive index sensors are highly sensitive and check for the basic evaluation parameters such as quality factor Q, and figure of merit (FOM). Furthermore, we have compared the proposed designs with previously published in a form of a table and presented them in Table 3.

IV. BEHAVIOR PREDICTION USING XGBoost REGRESSOR

Regression analysis is a machine learning approach to predict the value of a dependent variable using the value(s) of independent/correlated variable(s). Experiments are designed and performed using simulation data and XGBoost regressor to predict the absorption values for intermediate/missing frequency values. In these experiments, frequency is used as an independent variable and absorption value is used as a dependent variable.

A. XGBoost REGRESSOR

XGBoost is one of the most widely used and efficient Machine Learning methods of recent time. It uses a series of weak tree-based regressors with low efficiency to construct a strong regressor with high prediction performance [64]. Consider the dataset used to train the regression model is $D = \{\{x_i, y_i: i = 1 \text{ to } n\}$, here x_i is independent variable and y_i is a dependent variable (actual target value). XGBoost regressor uses equation (13) to compute the predicted target value

$$\bar{y}_i = \sum_{k=1}^{K} f_k(x_i), \quad f_k \in F \tag{13}$$

Here, f_k is k^{th} regression tree and $f_k(x_i)$ is the output of f_k for i^{th} input sample from dataset D and $\bar{y}_i$ is the predicted target value. The objective function of equation (14) is used to train

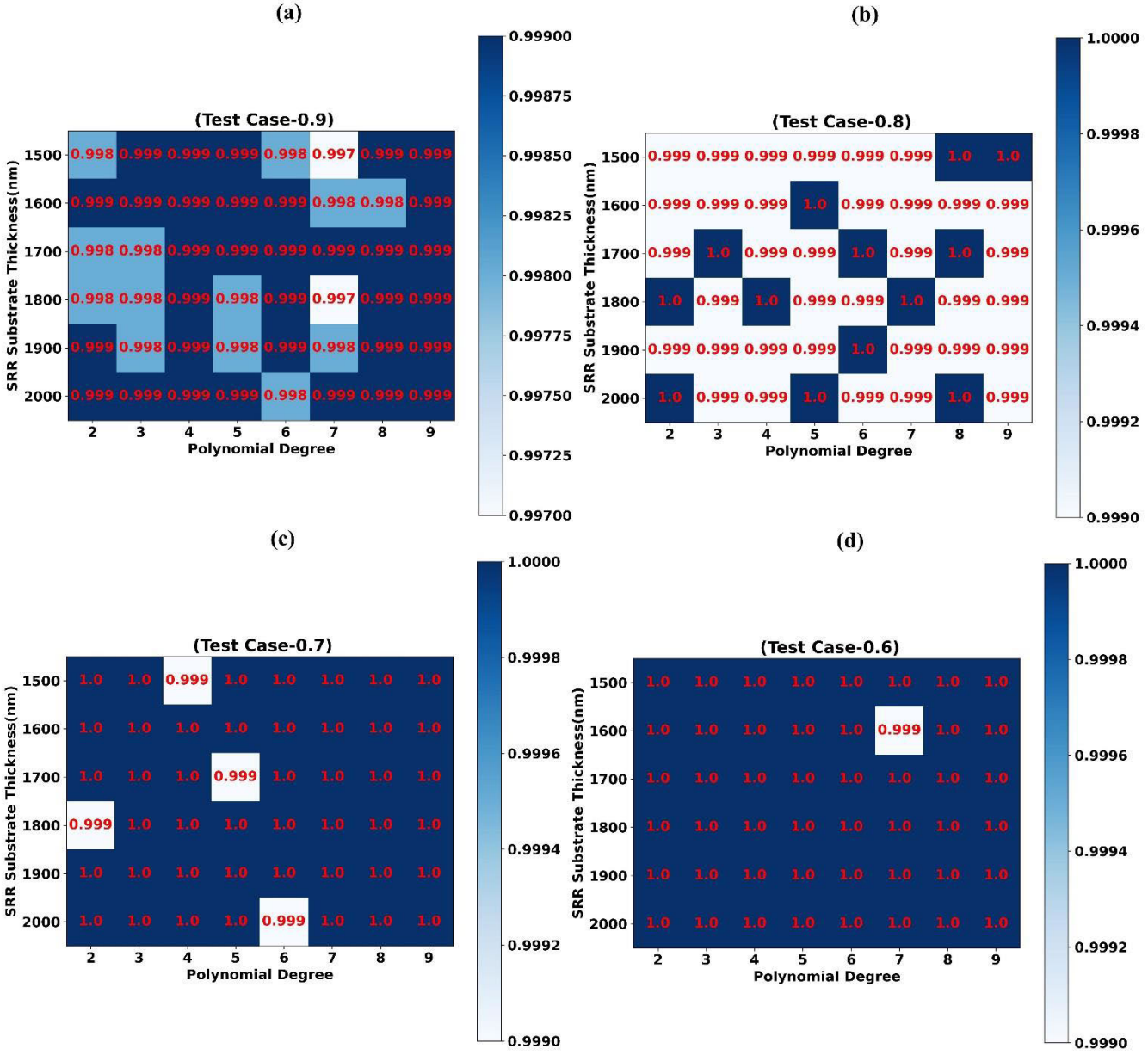

FIGURE 14. Prediction accuracy (R^2 Score) of XGBoost regressor models trained for various values of SRR substrate thickness and (a) Test Case T.C.-0.9 (b) Test Case T.C.-0.8 (c) Test Case T.C.-0.7 (d) Test Case T.C.-0.6.

the regression tree f_k.

$$Obj = \sum_{i=1}^{n} l\left(y_i, \bar{y}_i\right) + \sum_{k=1}^{K} \Omega(f_k) \tag{14}$$

$$\Omega\left(f_k\right) = \gamma T + \frac{1}{2}\lambda \left[\left[w\right]\right]^2 \tag{15}$$

Here, function 'l' computes the loss using actual, predicted value whereas λ and T are regularization arguments to avoid overfitting of the regressor model.

Covariance, Pearson's Correlation, Spearman's Correlation between frequency and absorption values for assorted SRR hemoglobin refractive index, SRR substrate thickness, SRR angle of incidence, SRR gap is shown in supplementary Fig. S1 (a-d) respectively. It indicates that linear correlation between frequency values and absorption values is absent and higher degree polynomial feature values of frequency must be used in the regression analysis process. Higher degree polynomial features for an independent variable 'X are calculated using equation (16).

$$[1, x_i^1, x_i^2, x_i^3, \ldots, x_i^m] \tag{16}$$

Here, m is the required degree of polynomial features. Statistical metric R^2 score is used to determine the prediction effectiveness of the XGBoost regressor. Equation (17) is used to compute the value of the R^2 score.

$$R^2 = 1 - \frac{SS_{red}}{SS_{tot}} \tag{17}$$

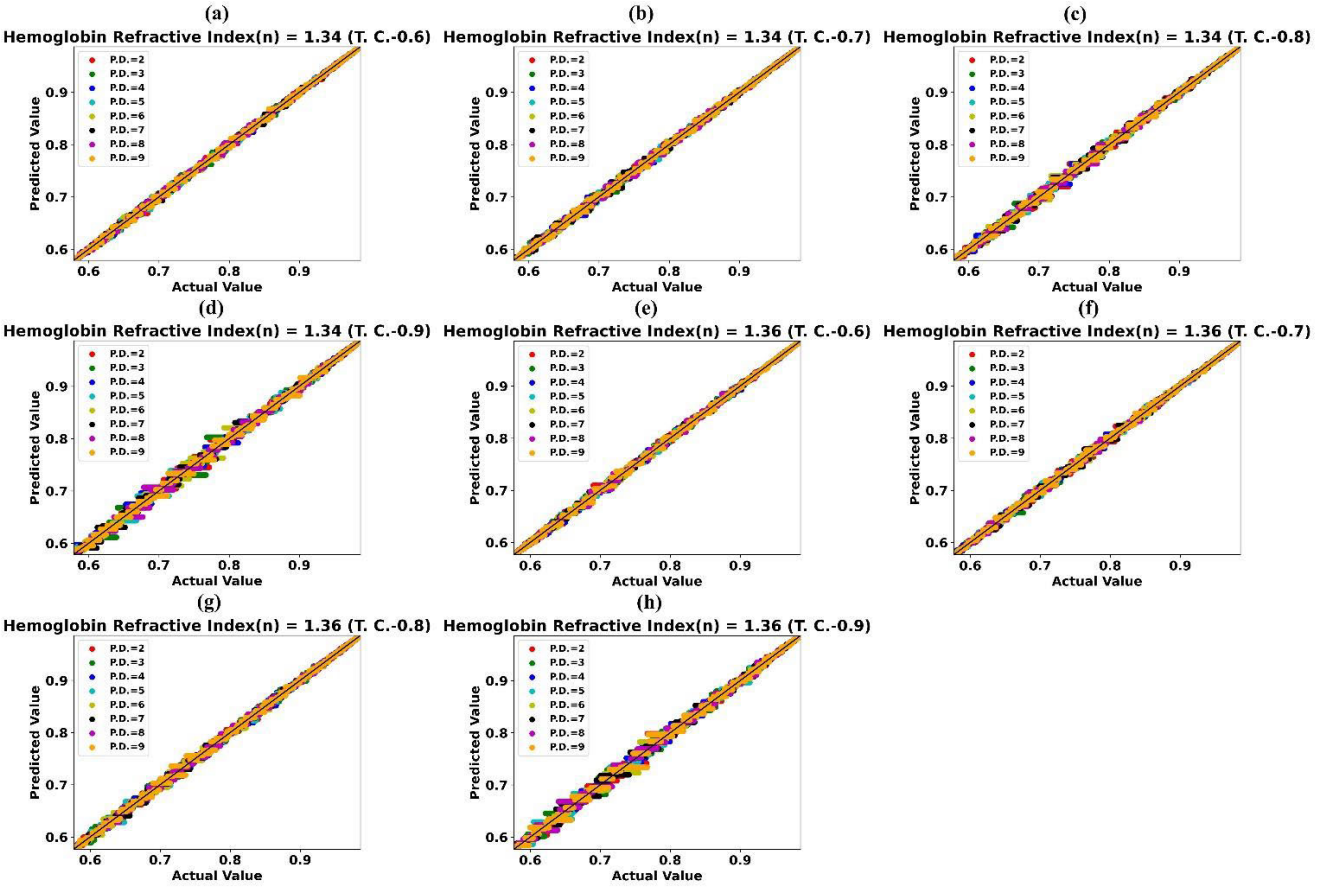

FIGURE 15. Predicted absorption value by XGBoost regressor vs. actual absorption value for SRR hemoglobin refractive index (n) (a) 1.34 (T.C.-0.6) (b) 1.34 (T.C.-0.7) (c) 1.34 (T.C.-0.8) (d) 1.34 (T.C.-0.9) (e) 1.36 (T.C.-0.6) (f) 1.36 (T.C.-0.7) (g) 1.36 (T.C.-0.8) (h) 1.36 (T.C.-0.9).

$$SS_{tot} = \sum_{i=1}^{N} (Actual\ Target_i - Average\ Target\ Value)^2 \quad (18)$$

$$SS_{red} = \sum_{1}^{N} (Predicted\ Target\ Value_i - Actual\ Target\ Value_i)^2 \quad (19)$$

XGoost Regressor models are implemented using Python 3.8, scikit machine learning library version 0.23.1, and xgboost library version 1.5.0. R2 score values are rounded off to 3 decimal places while presenting the results.

Four Test cases T.C.-0.6, T.C.-0.7, T.C.-0.8, and T.C.-0.9 are designed to evaluate the prediction effectiveness of the XGBoost regressor when it is trained using a minimum number of samples. In Test case T.C.-N, XGBoost regressor is trained using randomly selected (1-N) * 100 percentage of simulation samples, and prediction effectiveness of trained regressor is tested using remaining N*100 percentage simulation samples.

Scatter plots of predicted absorption values by XGBoost regressor vs actual absorption values obtained during simulation for SRR angle of incidence 0° and test cases T.C.-0.6, T.C.-0.7, T.C.-0.8, T.C.-0.9 are shown in Fig. 9 (a-d) respectively. Similarly, for SRR angle of incidence 10° and test cases T.C.-0.6, T.C.-0.7, T.C.-0.8, T.C.-0.9 are shown in Fig. 9 (e-h) respectively.

Prediction proficiency (R^2 Score) of XGBoost regressor models trained for various values of SRR angle of incidence and test cases T.C.-0.9, T.C.-0.8, T.C.-0.7, T.C.-0.6 is made known in Fig. 10 (a-d) respectively. It can be observed that, even though the regressor model is trained using only 10 percent of simulation samples (T.C. 0.9), it can predict the absorption values for the remaining 90 percent frequency values with high accuracy (more than or equal to 0.999 R^2 score). Whereas, when the regressor model is trained using 40 percent simulation samples (T.C.-0.6), it can predict the absorption values for remaining frequency values with extremely high accuracy (R^2 score of 1.0). These results show that the use of XGBoost regressor can reduce the simulation time and resources by at least 60 percent.

Scatter plots of predicted absorption values by XGBoost regressor vs actual absorption values obtained during simulation for SRR gap 500 nm (T.C.-0.6), 500 nm (T.C.-0.7), 500 nm (T.C.-0.8), 500 nm (T.C.-0.9), 1000 nm (T.C.-0.6), 1000 nm (T.C.-0.7), 1000 nm (T.C.-0.8), 1000 nm (T.C.-0.9) is shown in Fig. 11 (a-h) respectively.

Prediction proficiency (R^2 Score) of XGBoost regressor models trained for various values of SRR gap and test cases T.C.-0.9, T.C.-0.8, T.C.-0.7, T.C.-0.6 is made known in Fig. 12 (a-d) respectively. It can be observed that, even though

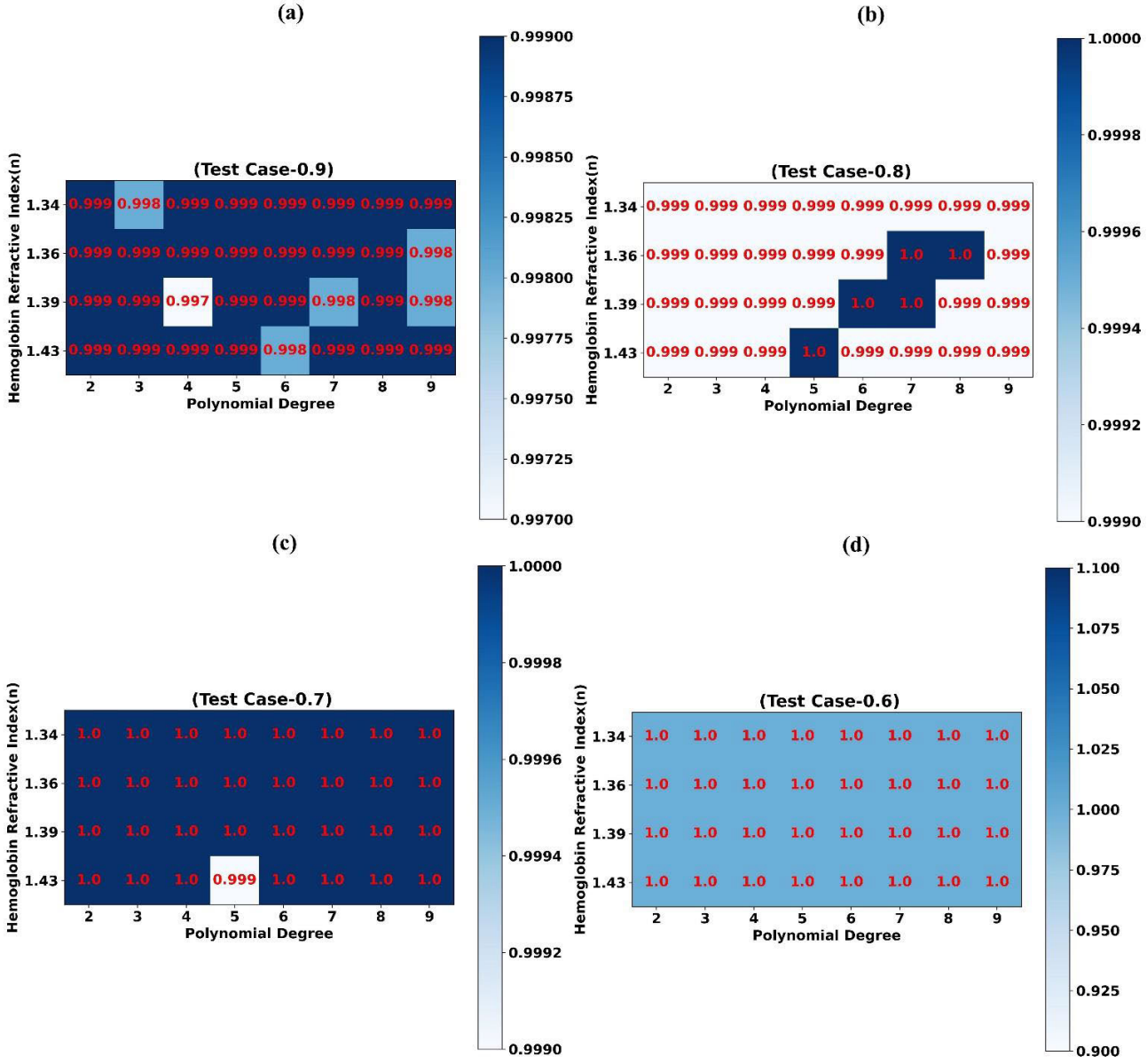

FIGURE 16. Prediction accuracy (R^2 Score) of XGBoost regressor models trained for various values of SRR hemoglobin refractive index and (a) Test Case T.C.-0.9 (b) Test Case T.C.-0.8 (c) Test Case T.C.-0.7 (d) Test Case T.C.-0.6.

the regressor model is trained using only 10 percent of simulation samples (T.C. 0.9), it can predict the absorption values for the remaining 90 percent frequency values with high accuracy (more than or equal to 0.999 R^2 score). Whereas, when the regressor model is trained using 30 percent simulation samples (T.C.-0.7), it can predict the absorption values for remaining frequency values with extremely high accuracy (R^2 score of 1.0). These results show that the use of XGBoost regressor can reduce the simulation time and resources by at least 70 percent.

Scatter plots of predicted absorption values by XGBoost regressor vs actual absorption values obtained during simulation for SRR substrate thickness 1500 nm (T.C.-0.6), 1500 nm (T.C.-0.7), 1500 nm (T.C.-0.8), 1500 nm (T.C.-0.9), 1600 nm (T.C.-0.6), 1600 nm (T.C.-0.7), 1600 nm (T.C.-0.8), 1600 nm (T.C.-0.9) is shown in Fig. 13 (a-h) respectively. Prediction proficiency (R^2 Score) of XGBoost regressor models trained for various values of SRR substrate thickness and test cases T.C.-0.9, T.C.-0.8, T.C.-0.7, T.C.-0.6 is made known in Fig. 14 (a-d) respectively. These results show that the use of XGBoost regressor can reduce the simulation time and resources by at least 70 percent.

Scatter plots of predicted absorption values by XGBoost Regressor vs actual absorption values for SRR hemoglobin refractive index 1.34 n (T.C.-0.6), 1.34 n (T.C.-0.7), 1.34 n (T.C.-0.8), 1.34 n (T.C.-0.9), 1.36 n (T.C.-0.6), 1.36 n (T.C.-0.7), 1.36 n (T.C.-0.8), 1.36 n (T.C.-0.9) is shown in Fig. 15 (a-h) respectively. Prediction proficiency (R^2 Score) of XGBoost regressor models trained for various values of hemoglobin concentration and test cases T.C.-0.9, T.C.-0.8,

T.C.-0.7, T.C.-0.6 is made known in Fig. 16 (a-d) respectively. These results show that the use of XGBoost regressor can reduce the simulation time and resources by at least 70 percent.

V. CONCLUSION

Three graphene-based refractive index sensors with different metasurface patterns of SRR, SRRTW, and TW are presented. Among these three designs, SRR and SRRTW can be used for encoding and tuning purposes due to their various plot for GCP values of 0.1 eV and 0.9 eV and frequency shift response w.r.t various concentrations of hemoglobin biomolecules. The SRR and SRRTW refractive index sensors achieved the highest sensitivity of 150 GHz/RIU and 133 GHz/RIU, respectively. The transmittance results are also then analyzed for various physical parameters and the results distinctly show that the frequency spectrum tunes for the variation in split ring gap, and angle of incidence. The results also indicate a slight tuning in frequency spectrum w.r.t substrate thickness of sensor. The electric field results also confirm the presented results of the sensor. The GCP is varied for 0.1 eV and 0.9 eV and can be encoded as '0' and '1', respectively. This concept then can be expanded by using an array of these types of sensors and applied in encoding and decoding-based applications. We have covered all the basic parameters defining the high quality of the sensor and we can conclude that the proposed sensors are highly sensitive and tunable based on the sensitivity, the figure of merit (FOM), and quality factor Q analysis. The proposed sensor with its tuning and encoding characteristics can be applied for biomedical and encoding-based applications. Experiments performed using XGBoost regressor prove that regression analysis using XGBoost Regressor can reduce the simulation time and resources by at least 70 percent. Experimental results further support that high prediction accuracy can be achieved (0.999 R^2 score) even if simulation time is reduced by 90 percent.

ACKNOWLEDGMENT

This work was supported by the Deanship of Scientific Research at Umm Al-Qura University under Grant 22UQU4170008DSR01.

DATA AVAILABILITY

The data will be made available at a reasonable request to the corresponding author.

CONFLICT OF INTEREST

The authors declare that they have no conflict of interest.

REFERENCES

[1] R. A. Shelby, D. R. Smith, and S. Schultz, "Experimental verification of a negative index of refraction," *Science*, vol. 292, no. 5514, pp. 77–79, Apr. 2001, doi: 10.1126/science.1058847.

[2] V. G. Veselago, "The electrodynamics of substances with simultaneously negative values of ϵ and μ" *Sov. Phys. Uspekhi*, vol. 10, no. 4, pp. 509–514, 1968, doi: 10.1070/pu1968v010n04abeh003699.

[3] C. M. Soukoulis, M. Kafesaki, and E. N. Economou, "Negative-index materials: New frontiers in optics," *Adv. Mater.*, vol. 18, no. 15, pp. 1941–1952, Aug. 2006, doi: 10.1002/adma.200600106.

[4] L.-X. Ran, H.-F. J. Tao, H. Chen, X.-M. Zhang, K.-S. Cheng, T. M. Grzegorczyk, and J. A. Kong, "Experimental study on several left-handed matamaterials," *Prog. Electromagn. Res.*, vol. 51, pp. 249–279, 2005, doi: 10.2528/PIER04040502.

[5] Y. Liu, Y. Ke, J. Zhou, H. Luo, and S. Wen, "Manipulating the spin-dependent splitting by geometric Doppler effect," *Opt. Exp.*, vol. 23, no. 13, p. 16682, Jun. 2015, doi: 10.1364/oe.23.016682.

[6] G. Presnova, D. Presnov, V. Krupenin, V. Grigorenko, A. Trifonov, I. Andreeva, O. Ignatenko, A. Egorov, and M. Rubtsova, "Biosensor based on a silicon nanowire field-effect transistor functionalized by gold nanoparticles for the highly sensitive determination of prostate specific antigen," *Biosensors Bioelectron.*, vol. 88, pp. 283–289, Feb. 2017, doi: 10.1016/j.bios.2016.08.054.

[7] S. Kumar, P. Goel, and J. P. Singh, "Flexible and robust SERS active substrates for conformal rapid detection of pesticide residues from fruits," *Sens. Actuators B, Chem.*, vol. 241, pp. 577–583, Mar. 2017, doi: 10.1016/j.snb.2016.10.106.

[8] H. Etayash, K. Jiang, S. Azmi, T. Thundat, and K. Kaur, "Real-time detection of breast cancer cells using peptide-functionalized microcantilever arrays," *Sci. Rep.*, vol. 5, no. 1, pp. 1–13, Nov. 2015, doi: 10.1038/srep13967.

[9] P. Singh, "SPR biosensors: Historical perspectives and current challenges," *Sens. Actuators B, Chem.*, vol. 229, pp. 110–130, Jun. 2016, doi: 10.1016/j.snb.2016.01.118.

[10] A. Zybin, V. Shpacovitch, J. Skolnik, and R. Hergenröder, "Optimal conditions for SPR-imaging of nano-objects," *Sens. Actuators B, Chem.*, vol. 239, pp. 338–342, Feb. 2017, doi: 10.1016/j.snb.2016.07.124.

[11] W. Xu, L. Xie, and Y. Ying, "Mechanisms and applications of terahertz metamaterial sensing: A review," *Nanoscale*, vol. 9, no. 37, pp. 13864–13878, 2017, doi: 10.1039/c7nr03824k.

[12] X. Yang, X. Zhao, K. Yang, Y. Liu, Y. Liu, W. Fu, and Y. Luo, "Biomedical applications of terahertz spectroscopy and imaging," *Trends Biotechnol.*, vol. 34, no. 10, pp. 810–824, Oct. 2016, doi: 10.1016/j.tibtech.2016.04.008.

[13] H.-R. Park, K. J. Ahn, S. Han, Y.-M. Bahk, N. Park, and D.-S. Kim, "Colossal absorption of molecules inside single terahertz nanoantennas," *Nano Lett.*, vol. 13, no. 4, pp. 1782–1786, Apr. 2013, doi: 10.1021/nl400374z.

[14] B. S. Alexandrov, V. Gelev, A. R. Bishop, A. Usheva, and K. Ø. Rasmussen, "DNA breathing dynamics in the presence of a terahertz field," *Phys. Lett. A*, vol. 374, no. 10, pp. 1214–1217, Feb. 2010, doi: 10.1016/j.physleta.2009.12.077.

[15] P. Zhao, S. Ragam, Y. J. Ding, and I. B. Zotova, "Compact and portable terahertz source by mixing two frequencies generated simultaneously by a single solid-state laser," *Opt. Lett.*, vol. 35, no. 23, p. 3979, Dec. 2010, doi: 10.1364/ol.35.003979.

[16] X. Yan, M. Yang, Z. Zhang, T. W. Wei, L. Liu, and J. Xie, "The terahertz electromagnetically induced transparency-like metamaterials for sensitive biosensors in the detection of cancer cells," *Biosensors Bioelectron.*, vol. 126, pp. 485–492, Feb. 2019, doi: 10.1016/j.bios.2018.11.014.

[17] Z. Zhang, M. Yang, X. Yan, X. Guo, J. Li, Y. Yang, D. Wei, L. Liu, J. Xie, Y. Liu, L. Liang, and J. Yao, "The antibody-free recognition of cancer cells using plasmonic biosensor platforms with the anisotropic resonant metasurfaces," *ACS Appl. Mater. Interfaces*, vol. 12, no. 10, pp. 11388–11396, Mar. 2020, doi: 10.1021/acsami.0c00095.

[18] P. Nie, D. Zhu, Z. Cui, F. Qu, L. Lin, and Y. Wang, "Sensitive detection of chlorpyrifos pesticide using an all-dielectric broadband terahertz metamaterial absorber," *Sens. Actuators B, Chem.*, vol. 307, Mar. 2020, Art. no. 127642, doi: 10.1016/j.snb.2019.127642.

[19] Y. Zhang, Y. Ye, X. Song, M. Yang, Y. Ren, X. Ren, L. Liang, and J. Yao, "High-sensitivity detection of chlorothalonil via terahertz metasensor," *Mater. Res. Exp.*, vol. 7, no. 9, Sep. 2020, Art. no. 095801, doi: 10.1088/2053-1591/aba805.

[20] J. Li, X. Huang, X. Zhao, L. Chen, and X. Yan, "PH-responsive torpedo-like persistent luminescence nanoparticles for autofluorescence-free biosensing and high-level information encryption," *Angew. Chem. Int. Ed.*, vol. 60, no. 5, pp. 2398–2405, Feb. 2021, doi: 10.1002/anie.202011553.

[21] M. Yang, H. Mei, Y. Shen, K. Wu, D. Pan, S. Liu, T. Zhang, and Y. Zhang, "Hot-tailoring of carbon nitride dots with redshifted photoluminescence for visual double text encryption and bioimaging," *Chem. Eur. J.*, vol. 25, no. 43, pp. 10188–10196, Aug. 2019, doi: 10.1002/chem.201901748.

[22] J. Parmar and S. K. Patel, "Encrypted and tunable graphene-based metasurface refractive index sensor," *Microw. Opt. Technol. Lett.*, vol. 64, no. 1, pp. 77–82, Jan. 2022, doi: 10.1002/mop.33049.

[23] E. Luan, H. Shoman, D. Ratner, K. Cheung, and L. Chrostowski, "Silicon photonic biosensors using label-free detection," *Sensors*, vol. 18, no. 10, p. 3519, Oct. 2018, doi: 10.3390/s18103519.

[24] A. Tavousi, M. R. Rakhshani, and M. A. Mansouri-Birjandi, "High sensitivity label-free refractometer based biosensor applicable to glycated hemoglobin detection in human blood using all-circular photonic crystal ring resonators," *Opt. Commun.*, vol. 429, pp. 166–174, Dec. 2018, doi: 10.1016/j.optcom.2018.08.019.

[25] S. Sang, Y. Wang, Q. Feng, Y. Wei, J. Ji, and W. Zhang, "Progress of new label-free techniques for biosensors: A review," *Crit. Rev. Biotechnol.*, vol. 36, no. 3, pp. 465–481, May 2016, doi: 10.3109/07388551.2014.991270.

[26] B. Xu, J. Huang, L. Ding, and J. Cai, "Graphene oxide-functionalized long period fiber grating for ultrafast label-free glucose biosensor," *Mater. Sci. Eng., C*, vol. 107, Feb. 2020, Art. no. 110329, doi: 10.1016/j.msec.2019.110329.

[27] R. Hernández, C. Vallés, A. M. Benito, W. K. Maser, F. X. Rius, and J. Riu, "Graphene-based potentiometric biosensor for the immediate detection of living bacteria," *Biosensors Bioelectron.*, vol. 54, pp. 553–557, Apr. 2014, doi: 10.1016/j.bios.2013.11.053.

[28] S. K. Patel, J. Parmar, Y. P. Kosta, M. Ladumor, R. Zakaria, T. K. Nguyen, and V. Dhasarathan, "Design of graphene metasurface based sensitive infrared biosensor," *Sens. Actuators A, Phys.*, vol. 301, Jan. 2020, Art. no. 111767, doi: 10.1016/j.sna.2019.111767.

[29] N. Pornsuwancharoen, M. A. Jalil, I. S. Amiri, J. Ali, and P. Yupapin, "Dual mode grating sensor using microring conjugate mirror and plasmonic island," *Microw. Opt. Technol. Lett.*, vol. 60, no. 10, pp. 2595–2599, 2018. [Online]. Available: https://onlinelibrary.wiley.com/doi/abs/10.1002/mop.31383, doi: 10.1002/mop.31383.

[30] S. K. Patel, J. Parmar, H. Trivedi, R. Zakaria, T. K. Nguyen, and V. Dhasarathan, "Highly sensitive graphene-based refractive index biosensor using gold metasurface array," *IEEE Photon. Technol. Lett.*, vol. 32, no. 12, pp. 681–684, Jun. 15, 2020, doi: 10.1109/LPT.2020.2992085.

[31] H. Vahed and C. Nadri, "Sensitivity enhancement of SPR optical biosensor based on Graphene–MoS2 structure with nanocomposite layer," *Opt. Mater.*, vol. 88, pp. 161–166, Feb. 2019, doi: 10.1016/j.optmat.2018.11.034.

[32] R. Jadeja, S. Charola, S. K. Patel, J. Parmar, M. Ladumor, T. K. Nguyen, and V. Dhasarathan, "Numerical investigation of graphene-based efficient and broadband metasurface for terahertz solar absorber," *J. Mater. Sci.*, vol. 55, no. 8, pp. 3462–3469, Mar. 2020, doi: 10.1007/s10853-019-04269-y.

[33] S. K. Patel, J. Parmar, D. Katrodiya, T. K. Nguyen, E. Holdengreber, and V. Dhasarathan, "Broadband metamaterial-based near-infrared absorber using an array of uniformly placed gold resonators," *J. Opt. Soc. Amer. B, Opt. Phys.*, vol. 37, no. 7, p. 2163, Jul. 2020, doi: 10.1364/josab.389283.

[34] J. Surve, J. Parmar, S. K. Patel, and R. Jadeja, "Comparative analysis of metasurface array-based solar absorber for visible region," *Opt. Quantum Electron.*, vol. 53, no. 12, p. 696, Dec. 2021, doi: 10.1007/s11082-021-03355-3.

[35] S. K. Patel and J. Parmar, "Highly sensitive and tunable refractive index biosensor based on phase change material," *Phys. B, Condens. Matter*, vol. 622, Dec. 2021, Art. no. 413357, doi: 10.1016/j.physb.2021.413357.

[36] L. Wang, Y. Zhang, A. Wu, and G. Wei, "Designed graphene-peptide nanocomposites for biosensor applications: A review," *Anal. Chim. Acta*, vol. 985, pp. 24–40, Sep. 2017, doi: 10.1016/j.aca.2017.06.054.

[37] S. K. Patel, J. Parmar, M. Ladumor, K. Ahmed, T. K. Nguyen, and V. Dhasarathan, "Numerical simulation of a highly directional optical leaky wave antenna using diamond-shaped graphene perturbations," *Appl. Opt.*, vol. 59, no. 8, p. 2225, Mar. 2020, doi: 10.1364/ao.386899.

[38] X. Zhao, J. Dong, E. Cao, Q. Han, W. Gao, Y. Wang, J. Qi, and M. Sun, "Plasmon-exciton coupling by hybrids between graphene and gold nanorods vertical array for sensor," *Appl. Mater. Today*, vol. 14, pp. 166–174, Mar. 2019, doi: 10.1016/j.apmt.2018.12.013.

[39] Z. Wang, Z. Geng, and W. Fang, "Exploring performance of THz metamaterial biosensor based on flexible thin-film," *Opt. Exp.*, vol. 28, no. 18, p. 26370, Aug. 2020, doi: 10.1364/oe.402222.

[40] S. K. Patel, J. Surve, J. Parmar, and T. K. Nguyen, "Review on graphene-based absorbers for infrared to ultraviolet frequencies," *J. Adv. Eng. Comput.*, vol. 5, no. 4, pp. 214–238, 2021.

[41] S. Barzegar-Parizi and A. Ebrahimi, "Ultrathin, polarization-insensitive multi-band absorbers based on graphene metasurface with THz sensing application," *J. Opt. Soc. Amer. B, Opt. Phys.*, vol. 37, no. 8, p. 2372, Aug. 2020, doi: 10.1364/josab.396266.

[42] S. Harnsoongnoen and A. Wanthong, "Coplanar waveguide transmission line loaded with electric-LC resonator for determination of glucose concentration sensing," *IEEE Sensors J.*, vol. 17, no. 6, pp. 1635–1640, Mar. 2017, doi: 10.1109/JSEN.2017.2652121.

[43] P. K. Varshney, A. Kapoor, and M. J. Akhtar, "Highly sensitive ELC resonator based differential sensor," *IEEE Trans. Instrum. Meas.*, vol. 70, pp. 1–10, 2021, doi: 10.1109/TIM.2021.3113135.

[44] F. Li, K. He, T. Tang, Y. Mao, R. Wang, C. Li, and J. Shen, "The terahertz metamaterials for sensitive biosensors in the detection of ethanol solutions," *Opt. Commun.*, vol. 475, Nov. 2020, Art. no. 126287, doi: 10.1016/j.optcom.2020.126287.

[45] O. Siddiqui, R. Ramzan, M. Amin, and O. M. Ramahi, "A non-invasive phase sensor for permittivity and moisture estimation based on anomalous dispersion," *Sci. Rep.*, vol. 6, no. 1, pp. 1–9, Sep. 2016, doi: 10.1038/srep28626.

[46] J. Homola, I. Koudela, and S. S. Yee, "Surface plasmon resonance sensors based on diffraction gratings and prism couplers: Sensitivity comparison," *Sens. Actuators B, Chem.*, vol. 54, nos. 1–2, pp. 16–24, Jan. 1999, doi: 10.1016/S0925-4005(98)00322-0.

[47] Z. Geng, X. Zhang, Z. Fan, X. Lv, and H. Chen, "A route to terahertz metamaterial biosensor integrated with microfluidics for liver cancer biomarker testing in early stage," *Sci. Rep.*, vol. 7, no. 1, pp. 1–11, Dec. 2017, doi: 10.1038/s41598-017-16762-y.

[48] G. W. Hanson, "Dyadic Green's functions and guided surface waves for a surface conductivity model of graphene," *J. Appl. Phys.*, vol. 103, no. 6, Mar. 2008, Art. no. 064302, doi: 10.1063/1.2891452.

[49] A. B. Numan and M. S. Sharawi, "Extraction of material parameters for metamaterials using a full-wave simulator [education column]," *IEEE Antennas Propag. Mag.*, vol. 55, no. 5, pp. 202–211, Oct. 2013, doi: 10.1109/MAP.2013.6735515.

[50] S. C. Bakshi, D. Mitra, and F. L. Teixeira, "Wide-angle broadband rasorber for switchable and conformal application," *IEEE Trans. Microw. Theory Techn.*, vol. 69, no. 2, pp. 1205–1216, Feb. 2021, doi: 10.1109/TMTT.2020.3044601.

[51] M. R. Rakhshani, "Wide-angle perfect absorber using a 3D nanorod metasurface as a plasmonic sensor for detecting cancerous cells and its tuning with a graphene layer," *Photon. Nanostruct.-Fundam. Appl.*, vol. 43, Feb. 2021, Art. no. 100883, doi: 10.1016/j.photonics.2020.100883.

[52] M. Pan, H. Huang, B. Fan, W. Chen, S. Li, Q. Xie, F. Xu, D. Wei, and J. Fang, "Theoretical design of a triple-band perfect metamaterial absorber based on graphene with wide-angle insensitivity," *Results Phys.*, vol. 23, Apr. 2021, Art. no. 104037, doi: 10.1016/j.rinp.2021.104037.

[53] J. Xu, R. Li, J. Qin, S. Wang, and T. Han, "Ultra-broadband wide-angle linear polarization converter based on H-shaped metasurface," *Opt. Exp.*, vol. 26, no. 16, p. 20913, Aug. 2018, doi: 10.1364/oe.26.020913.

[54] S. Patel, J. Parmar, V. Sorathiya, R. Zakaria, T. K. Nguyen, and V. Dhasarathan, "Graphene-based plasmonic absorber for biosensing applications using gold split ring resonator metasurfaces," *J. Lightw. Technol.*, vol. 39, no. 17, pp. 5617–5624, Sep. 1, 2021, doi: 10.1109/JLT.2021.3069758.

[55] R. Singh, W. Cao, I. Al-Naib, L. Cong, W. Withayachumnankul, and W. Zhang, "Ultrasensitive terahertz sensing with high-Q Fano resonances in metasurfaces," *Appl. Phys. Lett.*, vol. 105, no. 17, Oct. 2014, Art. no. 171101, doi: 10.1063/1.4895595.

[56] S. Sahu, J. Ali, P. P. Yupapin, and G. Singh, "Porous silicon based Bragg-grating resonator for refractive index biosensor," *Photonic Sensors*, vol. 8, no. 3, pp. 248–254, Sep. 2018, doi: 10.1007/s13320-018-0459-z.

[57] Z. Wei, X. Li, N. Zhong, X. Tan, X. Zhang, H. Liu, H. Meng, and R. Liang, "Analogue electromagnetically induced transparency based on low-loss metamaterial and its application in nanosensor and slow-light device," *Plasmonics*, vol. 12, no. 3, pp. 641–647, Jun. 2017, doi: 10.1007/s11468-016-0309-z.

[58] X.-J. He, L. Wang, J.-M. Wang, X.-H. Tian, J.-X. Jiang, and Z.-X. Geng, "Electromagnetically induced transparency in planar complementary metamaterial for refractive index sensing applications," *J. Phys. D, Appl. Phys.*, vol. 46, no. 36, Sep. 2013, Art. no. 365302, doi: 10.1088/0022-3727/46/36/365302.

[59] M. Wan, S. Yuan, K. Dai, Y. Song, and F. Zhou, "Electromagnetically induced transparency in a planar complementary metamaterial and its sensing performance," *Optik*, vol. 126, no. 5, pp. 541–544, Mar. 2015, doi: 10.1016/j.ijleo.2015.01.006.
[60] S. K. Patel, J. Parmar, H. Trivedi, R. Zakaria, T. K. Nguyen, and V. Dhasarathan, "Highly sensitive graphene-based refractive index biosensor using gold metasurface array," *IEEE Photon. Technol. Lett.*, vol. 32, no. 12, pp. 681–684, Jun. 15, 2020, doi: 10.1109/LPT.2020.2992085.
[61] S. Sahu, J. Ali, P. P. Yupapin, and G. Singh, "Optical biosensor based on a cladding modulated grating waveguide," *Optik*, vol. 166, pp. 103–109, Aug. 2018, doi: 10.1016/j.ijleo.2018.04.034.
[62] G. An, S. Li, T. Cheng, X. Yan, X. Zhang, X. Zhou, and Z. Yuan, "Ultra-stable D-shaped optical fiber refractive index sensor with graphene-gold deposited platform," *Plasmonics*, vol. 14, no. 1, pp. 155–163, Feb. 2019, doi: 10.1007/s11468-018-0788-1.
[63] S. Olyaee, S. Najafgholinezhad, and H. Alipour Banaei, "Four-channel label-free photonic crystal biosensor using nanocavity resonators," *Photon. Sensors*, vol. 3, no. 3, pp. 231–236, Sep. 2013, doi: 10.1007/s13320-013-0110-y.
[64] T. Chen and C. Guestrin, "XGBoost: A scalable tree boosting system," in *Proc. 22nd ACM SIGKDD Int. Conf. Knowl. Discovery Data Mining*, Aug. 2016, pp. 785–794, doi: 10.1145/2939672.2939785.

SHOBHIT K. PATEL (Senior Member, IEEE) received the Ph.D. degree in electronics and communication engineering from the Charotar University of Science and Technology, Changa, India. He is currently working in the area of photonics, metamaterial, antenna, optics, and artificial intelligence. He has published several research papers in high impact SCI journals. He has also filed seven Indian patents on different novel research done by him. He received the DST International Travel Grant, in 2014, to present a paper in IEEE APS-URSI Symposium, Memphis, USA. He also received the DST International Travel Grant, in 2017, to present a paper in PIERS Symposium, NTU, Singapore. He has been named in the list of "top 2% scientist worldwide identified by Stanford University," in 2021. He is currently working on many graphene-based projects and has received funding from SERB, DST, for his research. He has been honored with awards for the achievements in the area of the research field.

JAYMIT SURVE (Graduate Student Member, IEEE) received the B.Tech. degree in electrical engineering from the Institute of Infrastructure Technology Research and Management, Ahmedabad, and the M.E. degree in electrical engineering with specialization in automatic control and robotics from The Maharaja Sayajirao University of Baroda, Vadodara. He has recently joined Marwadi University as a Junior Research Fellow, in July 2021. His recent research interests include multidisciplinary research in the field of absorbers, sensors, graphene, robotics, and AI-based disaster management for search and rescue missions.

VIJAY KATKAR received the B.E. degree in information technology and the M.Tech. degree in computer engineering from the University of Mumbai, India, in 2005 and 2008, respectively, and the Ph.D. degree in computer engineering from Bharati Vidyapeeth, Pune, India, in 2017. Currently, he is working as an Associate Professor with the Computer Engineering Department, Marwadi University, Rajkot, India. He has more than 30 publications in international journals and conferences. His research interests include networks security, machine learning, and computer vision.

JUVERIYA PARMAR (Graduate Student Member, IEEE) received the B.Sc. degree in physics from Saurashtra University and the M.Sc. degree in physics from Marwadi University. She has recently joined as a Graduate Research Assistant at the University of Nebraska–Lincoln, Lincoln, NE, USA. Before joining the University of Nebraska–Lincoln, she was an employee of Marwadi University for two years, where she worked in the field of graphene, metamaterials, biosensors, and solar absorbers. She is currently working in the field of photonics, electromagnetics, and materials. She has published more than 27 SCI articles in international journals.

FAHAD AHMED AL-ZAHRANI received the B.Sc. degree in electrical and computer engineering from Umm Al-Qura University, Mecca, Saudi Arabia, in 1996, the M.S. degree in computer engineering from the Florida Institute of Technology, in 2000, and the Ph.D. degree in computer engineering from Colorado State University, in 2005. He has taught several computer network courses and supervised related research projects. From 2011 to 2016, he was the IT Dean at Umm Al-Qura University and has had several other responsibilities thereafter, where he is currently a Professor with the Computer Engineering Department. His research interests include high-speed network protocols, sensor networks, optical networks, performance evaluation, the IoT, and blockchain architecture and performance analysis. He is a member of the International Society for Optical Engineering and the Optical Society of America.

KAWSAR AHMED (Graduate Student Member, IEEE) received the B.Sc. and M.Sc. (Engineering) degrees in information and communication technology (ICT) from Mawlana Bhashani Science and Technology University, Tangail, Bangladesh. He is currently pursuing the Ph.D. degree in biomedical engineering with the University of Saskatchewan, Canada. He is also serving as an Assistant Professor with Mawlana Bhashani Science and Technology University, Tangail, Bangladesh. Prior to that, he joined the Software Engineering Department, Daffodil International University, as a Lecturer. He has more than 250 publications in IEEE, IET, OSA, Elsevier, Springer, ISI, and PubMed indexed journals. He has published two books on bioinformatics and photonic sensor design. He is a Research Coordinator of the "Group of Biophotomatiχ." His research interests include biomedical engineering, biophotonics, biosensor, machine learning, federated learning, data mining, and bioinformatics. He is also a member of SPIE and OSA. He holds the top position at his department as well as in university and is listed among the top 10 researchers in Bangladesh, from 2020 to 2017 (Scopus indexed-based). His research group received the SPIE Travelling Award and the Best Paper Award at the IEEE WIECON ECE-2015 Conference. He has achieved gold medals for engineering faculty first both in B.Sc. and M.Sc. degrees from Mawlana Bhashani Science and Technology University for his academic excellence.

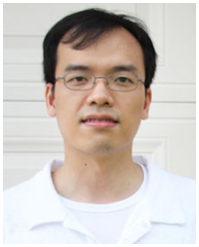

FRANCIS MINHTHANG BUI (Member, IEEE) received the B.A. degree in French language and the B.Sc. degree in electrical engineering from the University of Calgary, Canada, in 2001, and the M.Sc. and Ph.D. degrees in electrical engineering from the University of Toronto, Canada, in 2003 and 2009, respectively. He is currently an Associate Professor of electrical and computer engineering with the University of Saskatchewan, Canada. His research interests include information processing and machine learning, with applications in communications and biomedical engineering.